Experimental investigation of total bottom shear stress for oscillatory flows over sand ripples

Jing Yuan[1], Dongxu Wang[1]

[1]Department of Civil and Environmental Engineering, National University of Singapore, Singapore

Key Points.

A pressure-based technique is developed for measuring total bottom shear stress over wave-generated vortex ripples.

Total bottom shear stress is dominated by its first-harmonic Fourier component, which is almost in-phase with the free-stream velocity.

Investigated the equivalent sand grain roughness for predicting total wave bottom shear stress over rippled bed.

Abstract. Shoaling waves often produce vortex ripples on a sandy seabed, which significantly increases the local bottom shear stress. To improve the quantitative understanding of this phenomenon, a full-scale experimental study is conducted using an oscillatory water tunnel. In the tests, sinusoidal oscillatory flows generate 2 dimensional uniform sand ripples from a 9 m-long movable bed made of coarse sand. The total bottom shear stress is estimated from the change of water pressure for driving the oscillatory flow. Flow around individual ripples are also measured using Particle Image Velocimetry. After correction for imperfect flow generation and facility vibration, the leading three odd harmonics of total bottom shear stress are kept in the final measurements. The first harmonic is the dominant one, and is generally in-phase with the free-stream velocity. Its amplitude decreases as ripples are washed-off by increasing flow intensity. The third and the fifth harmonics are about 10-20% of the first harmonic in amplitude. Their presence make the intra-period variation of total bottom shear stress quite wavy with three peaks within one half-period. Flow measurements suggest that these peaks are closely related to coherent vortex motions. For two selected tests, total bottom shear

stress is estimated from velocity measurements via a control-volume analysis. The results are in good agreement with those from the pressure-based technique, which verifies both approaches. A new predictor for the equivalent sand grain roughness in *Humbyrd* [2012]'s formula for wave friction factor is calibrated based on the obtained measurements of maximum total bottom shear stress.

1. Introduction

Moderate shoaling waves can generate some small-scale bedforms on a sandy seabed, i.e. sand ripples, which are typically 1∼10 cm high and 10∼100 cm long. The pioneering work of *Bagnold and Taylor* [1946] showed that wave-induced flow over sand ripples is characterized by coherent vortices, which are alternately produced on both sides of ripple crest under the oscillatory free-stream motion, so wave-generated sand ripples are also known as vortex ripples. The coherent vortices lead to significant spatial inhomogeneity of local boundary layer flow [e.g., *Nichols and Foster*, 2007; *van der Werf et al.*, 2007], which alters the pressure distribution on the ripple surface. As a result, a ripple-averaged pressure force in the streamwise direction is produced, which is often referred to as form drag. Form drag is usually much stronger than the skin friction (surface shear stress), so the presence of vortex ripples significantly enhances the local flow resistance. *Kajiura* [1968] showed that the energy dissipation rate for wave boundary layer is given by period-averaging the product of total bottom shear stress (total flow resistance per unit surface area) and free-stream velocity. Therefore, vortex ripples also increase the local energy dissipation rate, which is reflected in the attenuation of surface waves [e.g., *Nielsen*, 1983].

The maximum wave bottom shear stress is of primary interest, and it is conventionally expressed as a wave friction factor f_w. Many experimental studies over the past decades aimed at measuring f_w for oscillatory flows over vortex ripples. Most studies indirectly inferred f_w from measurements of energy dissipation rate, which can be estimated by measuring wave height attenuation as waves travel over a rippled bed in laboratory wave flumes [e.g., *Rosengaus*, 1987; *Mathisen*, 1989]. A rather unique study was reported by

Carstens et al. [1969], in which the energy dissipation was inferred from the input energy for driving oscillatory flows in an oscillatory water tunnel (OWT). There are a few studies, which measured energy dissipation rate in the field [e.g., *Treloar and Abernethy*, 1978], but the measurement error can be quite significant. The key disadvantage of all energy-dissipation-based studies is that a temporal variation of total bottom shear stress must be pre-assumed, such as a sinusoidal variation, which may be incorrect. Experiments, which directly report the total flow resistance, are quite few. In the wave tank experiments of *Rankin and Hires* [2000], vortex ripples are generated on a shear plate, so the total flow resistance can be directly measured and the maximum value is translated to f_w. *Lofquist* [1980] reported an OWT study, in which the test channel is partitioned into two channels along its longitudinal centerline. One channel has a flat bed and the other has a rippled bed. A piston drives the same oscillatory flow in both channels, so the difference in piston-end driving pressure is due to form drag over vortex ripples. This, to the authors' knowledge, is perhaps the only experiment, which reports the intra-period variation of total bottom shear stress. *Lofquist* [1980]'s measurements suggest that the bottom shear stress has two peaks within half of a flow cycle, one before and the other after the maximum free-stream velocity. Some recent experimental studies were able to capture the detailed flow field around individual vortex ripples, so some researchers attempted to estimate f_w from velocity measurements [e.g., *Hay et al.*, 2012; *Hare et al.*, 2014; *Rodríguez-Abudo and Foster*, 2017]. Among these studies, certain assumption must be adopted to estimate f_w. For instance, *Rodríguez-Abudo and Foster* [2017] assumed that the momentum transfer rate at the ripple crest level follows a quadratic law scaled by f_w. Due to limited facility sizes, most previous studies (both direct or indirect mea-

surements) are usually not corresponding to full-scale conditions, so more experimental effort is required to further elucidate this challenging topic.

Wave friction factor (or bottom shear stress) can be predicted with simple empirical formula [e.g., *Jonsson*, 1966; *Swart*, 1974], theoretical [e.g., *Madsen*, 1994] or advanced numerical [e.g., *Holmedal et al.*, 2003] models. Following the classical work of *Nikuradse* [1933], an equivalent sand-grain roughness is commonly adopted for describing a rough bed. Thus, many research efforts have been directed towards quantifying the bottom roughness for vortex ripples. Intuitively, it makes sense to relate bottom roughness to ripple dimension (height and length). Bottom roughness can be back-calculated with a wave friction factor formula and the measurements of f_w, while ripple dimension can be directly measured, so a number of predictors of bottom roughness have been calibrated. Some researchers proposed that bottom roughness is simply proportional to ripple height [e.g., *Wikramanayake and Madsen*, 1994], while others prefer a bottom roughness proportional to the product of ripple height and ripple steepness (height divided by length) [e.g., *Grant and Madsen*, 1982; *Nielsen*, 1983]. Depending on the selected dataset and the adopted wave boundary layer model, the discrepancy among various predictors can be quite dramatic.

To directly predict total bottom shear stress over vortex ripples, theoretical models must be able to resolve the coherent vortex motion. *Longuet-Higgins* [1981] proposed an inviscid discrete vortex model, which assumes that flow always separates at ripple crest. *Sleath* [1982] solved the finite difference form of the vorticity equation to obtain total flow resistance. These early works do not appropriately account for turbulence, so they may not work well for prototype flow conditions. *Fredsøe et al.* [1999] numerically solved

the Reynolds-Averaged Navier-Stokes (RANS) equation with a $k-\omega$ model for turbulence closure. *Barr et al.* [2004] and *Grigoriadis et al.* [2012], among others, performed Large-Eddy Simulation (LES) of oscillatory flows over vortex ripples. To avoid the need for turbulence closure models, some numerical studies, e.g., *Scandura et al.* [2000] and *Blondeaux et al.* [2004], adopted Direct Numerical Simulation (DNS), but this technique is computationally too expensive to reach field-scale Reynolds numbers. Direct measurements of total bottom shear stress, especially for full-scale conditions, are required to validate these numerical models.

In this study, a pressure-based technique is developed for directly measuring total flow resistance for vortex ripples developed in an OWT. The test conditions correspond to full-scale simulations of wave-driven near-bed flows, and two-dimensional equilibrium vortex ripples are obtained in all tests. The new experimental results reveal the intra-period variation of total bottom shear stress. The maximum total bottom shear stress is subsequently used to calibrate a new bottom roughness predictor. Section 2 presents the theoretical background of the experimental methodology and the experimental setup. Section 3 discusses the data analysis procedure. Experimental results are shown in Section 4. The bottom roughness predictor is presented in Section 5, and conclusions are provided in Section 6.

2. Experimental methodology

2.1. Total bottom shear stress for oscillatory flow over 2D uniform vortex ripples

As a simple approximation of wave boundary layer over a ripped bed, we consider sinusoidal oscillatory flows over 2-dimensional uniform vortex ripples, so the free-stream

velocity is

$$u_\infty(t) = U_\infty \cos\omega t = U_\infty \cos\theta \tag{1}$$

where U_∞ is the amplitude, θ is the phase angle and $\omega = 2\pi/T$ is the radian frequency with T being the period. Oscillatory boundary layer flows produce pressure and shear stress on the surface of vortex ripples, so the total force acting on a whole ripple is

$$F_R = \int_0^\lambda \frac{p_\eta}{\rho}\frac{\partial \eta}{\partial x}dx + \int_0^\lambda \frac{\tau_\eta}{\rho}dx \tag{2}$$

where ρ is water density, x is the horizontal coordinate, λ is ripple length, η is the vertical coordinate of the ripple surface, p_η and τ_η are pressure and bottom shear stress acting on the ripple surface, respectively. Conventionally, the started point of the integral, $x = 0$, is a ripple trough (see figure 1). It should be noted that F_R is not independent of where $x = 0$ is. To show this, we write p_η as

$$p_\eta = p_\infty + p' \tag{3}$$

where p_∞ is associated with free-stream flow, i.e.,

$$\frac{\partial u_\infty}{\partial t} = -\frac{1}{\rho}\frac{\partial p_\infty}{\partial x} \tag{4}$$

and p' is the difference between p_η and p_∞. For uniform 2D ripples, p' should be periodic in x, while p_∞ varies linearly with x, according to equation (4). We can subsequently split the first term on the right-hand side of equation (2), into two terms related to p' and p_∞, respectively. The p_∞-related term can be further written as

$$F_I = \int_0^\lambda \frac{p_\infty}{\rho}\frac{\partial \eta}{\partial x}dx = \frac{\partial u_\infty}{\partial t}\left(\int_0^\lambda \eta dx - \eta_0\lambda\right) \tag{5}$$

where η_0 is the bottom level at $x = 0$. F_I is in-phase with the acceleration of free-stream velocity, so it can be considered as an inertial-related pressure force. F_I is always 90° out

of phase with u_∞, so it will not cause any energy dissipation. Apparently, the value of F_I depends on the value of η_0, as pointed out by *Sleath* [1982]. Note that p' is due to the negotiation of boundary layer flow and the wavy bottom, e.g., it captures the effect of flow separation at ripple crest. As will be demonstrated by our experimental results, this term is mostly in-phase with the free-stream velocity, so it can be considered as drag-related pressure force (denoted as F_D)

$$F_D = \int_0^\lambda \frac{p'}{\rho}\frac{\partial \eta}{\partial x}dx = \int_0^\lambda \frac{(p_\eta - p_\infty)}{\rho}\frac{\partial \eta}{\partial x}dx. \tag{6}$$

F_D is directly related to the boundary layer processes and contributes to the energy dissipation rate (the main contributor). Also, since p' is periodic in x, F_D does not depend on where $x = 0$ is.

The immediate question is how to treat F_I. For coastal-engineering applications, two key aspects regarding sand ripples are energy dissipation and turbulent mixing of momentum and sediment in close vicinity of the ripple surface. As discussed before, F_I has no contribution to the energy dissipation rate, and it is irrelevant for turbulent mixing, since p_∞ is not affected by coherent vortex motion or boundary-layer turbulence. Therefore, it is reasonable to remove F_I from the definition of total flow resistance. This will also bypass the problem of choosing $x = 0$. Note that this is also the choice in the similar experimental investigation by *Lofquist* [1980]. The total bottom shear stress, τ_b, is the total flow resistance averaged over one ripple length, which is conventionally split into a form-drag bottom shear stress, τ_F, and a skin-friction bottom shear stress, τ_S, i.e.

$$\tau_b = \tau_F + \tau_s = \frac{1}{\lambda}\int_0^\lambda \frac{p_\eta - p_\infty}{\rho}\frac{\partial \eta}{\partial x}dx + \frac{1}{\lambda}\int_0^\lambda \frac{\tau_\eta}{\rho}dx. \tag{7}$$

2.2. Research facility and measurement method

In this study, experiments are conducted using the Wave-Current-Sediment (WCS) facility [see *Yuan and Madsen*, 2014] at the hydraulic lab of National University of Singapore. The WCS is essentially an oscillatory water tunnel. As shown in figure 2a, it consists of a horizontal enclosed test section connected to two vertical cylindrical risers. A hydraulic piston is located in one riser, and the other riser is open to the atmosphere, so the piston can drive uniform oscillatory flows in the test section. The test section is 9 m-long, 40 cm-wide and 50 cm-deep, and there is a 20 cm-deep trough for holding sediments. Each end of the test section is connected to a honeycomb flow filter through a 1 m-long transition, which has a rigid steel bottom. Assuming 2-dimensional flow in the test section, the governing equation for momentum in the horizontal direction is

$$\frac{\partial u}{\partial t} + u\frac{\partial u}{\partial x} + w\frac{\partial u}{\partial z} = \frac{1}{\rho}\left(-\frac{\partial p}{\partial x} + \frac{\partial \tau_{xx}}{\partial x} + \frac{\partial \tau_{xz}}{\partial z}\right) \tag{8}$$

where u and w are horizontal and vertical components of flow velocity, respectively, τ_{xx} and τ_{zx} are shear stresses, and x and z are horizontal and vertical coordinates, respectively. The continuity equation is

$$\frac{\partial u}{\partial x} + \frac{\partial w}{\partial z} = 0. \tag{9}$$

We assume that the bottom is fixed and impermeable, so a no-slip boundary condition is applied at the bottom, $z = \eta$. We integrate equation (8) from the bottom to the top of test section $z = h$. With the assumption that $p \gg \tau_{xx}$ the following depth-integrated momentum equation is obtained

$$\frac{\partial q}{\partial t} + \frac{\partial}{\partial x}\int_\eta^h u^2 dz = -\frac{\partial}{\partial x}\int_\eta^h \frac{p}{\rho} dz - \frac{p_\eta}{\rho}\frac{\partial \eta}{\partial x} + \frac{\tau_h}{\rho} - \frac{\tau_\eta}{\rho} \tag{10}$$

where τ_h is the shear stress acting on the top lid, p_η and τ_η are the pressure and the shear stress acting on the bottom, and q is the discharge rate per unit channel width, which is defined as

$$q = \int_\eta^h u dz. \tag{11}$$

Assuming that the ripples in the test section are stationary, conservation of water volume requires that q is not a function of x. Equation (10) can be integrated from x_0 to x_L, where x_0 and x_L are located somewhere within the 1 m-long transitions outside the movable bed (see figure 2a), which gives

$$(x_L - x_0)\frac{\partial q}{\partial t} + \int_\eta^h u^2 dz\Big|_{x_0}^{x_L} = -\int_\eta^h \frac{p}{\rho} dz\Big|_{x_0}^{x_L} - F_B + \int_{x_0}^{x_L} \frac{\tau_h}{\rho} dx \tag{12}$$

where

$$F_B = F_{Bp} + F_{Bs} = \int_{x_0}^{x_L} \frac{p_\eta}{\rho}\frac{\partial \eta}{\partial x} dx + \int_{x_0}^{x_L} \frac{\tau_\eta}{\rho} dx \tag{13}$$

is the total force (including pressure F_{Bp} and skin-friction F_{Bs}) from the bottom and the last term on the right-hand side of equation (12) represents the total shear force from the top lid. Since the flows at x_0 and x_L can be assumed identical, the second term on the left-hand side of equation (12) is negligible. Also, the pressure at x_0 and x_L should vary in a hydrostatic manner in the z-direction, since the local flow is parallel to the flat steel bottom. Thus, the first term on the right-hand side of equation (12) can be written as

$$-\int_\eta^h \frac{p}{\rho} dz\Big|_{x_0}^{x_L} = \frac{h}{\rho}\left(p_{h0} - p_{hL}\right) \tag{14}$$

where p_{h0} and p_{hL} are the water pressure under the top lid at x_0 and x_L, respectively. Note that p_{hL} drives the flow from the free water surface in the open riser to $x = x_L$, so it does not depend on the bottom condition inside the test section. In other words, p_{hL} is

the same for tests with the same flow condition. With this information, we can re-write equation (12) as

$$\frac{h}{\rho}\left(p_{h0}-p_{hL}\right)=(x_L-x_0)\frac{\partial q}{\partial t}+F_B+\int_{x_0}^{x_L}\frac{\tau_h}{\rho}dx \tag{15}$$

For two tests with the same flow condition but different bottom configurations (one with flat bed and the other with a rippled bed), only p_{h0} and F_B will change, so subtracting the momentum equation for a rippled bed from that for a flat bed leads to

$$\frac{h}{\rho}\left(p_{h0,r}-p_{h0,f}\right)=\frac{h}{\rho}\Delta p=F_{B,r}-F_{B,f} \tag{16}$$

where the subscripts "r" and "f" denote rippled- and flat-bed conditions, respectively, and Δp is the change of water pressure under the lid at $x=x_0$. $F_{B,f}$ can be fairly estimated with a prediction of bottom shear stress ($\tau_{b,f}$) on the flat bed, i.e., $F_{B,f}=\tau_{b,f}L$, where L is the length of the test section. *Yuan and Madsen* [2014] experimentally shows that $\tau_{b,f}$ of sinusoidal oscillatory flows over a rough surface can be obtained as the superposition of a first and a third harmonics, i.e.,

$$\tau_{b,f}(t)=\frac{1}{2}\alpha f_w\rho {U_\infty}^2\cos(\omega t+\varphi_{\tau b})+\frac{1}{2}(1-\alpha)f_w\rho {U_\infty}^2\cos(3\omega t+3\varphi_{\tau b}) \tag{17}$$

where $\alpha\approx 0.87$ and the friction factor f_w and phase lead $\varphi_{\tau b}$ can be accurately evaluated with the wave boundary layer model proposed by *Humbyrd* [2012]. Thus, the total bottom shear stress for a rippled bed, which is defined as $\tau_b=F_{B,r}/L$, can be evaluated with the measurement of Δp and the prediction of $\tau_{b,f}$, i.e.,

$$\tau_b=\frac{h}{L}\Delta p+\tau_{b,f}\approx\tau_F+\tau_S. \tag{18}$$

It is reasonable to assume that the skin-friction bottom shear stress, τ_S, is the same for both bed conditions, so $\tau_{b,f}$ can be approximately considered as τ_S, then $h\Delta p/L$, which is

what will be measured, is essentially the form-drag bottom shear stress, τ_F. Equation (18) is the basis for our experimental methodology.

It should be highlighted that the total bottom shear stress obtained from equation (18) is without the inertial-related pressure force defined in equation (5). To show this, we can write the pressure force over the entire rippled bed as

$$\int_{x_0}^{x_L} \left(\frac{p_\eta}{\rho} \frac{\partial \eta}{\partial x} \right) dx = \int_{x_0}^{x_L} \left(\frac{p_\infty}{\rho} \frac{\partial \eta}{\partial x} \right) dx + \int_{x_0}^{x_L} \left(\frac{p'}{\rho} \frac{\partial \eta}{\partial x} \right) dx. \tag{19}$$

Here we define $\eta = 0$ at $x = x_0$ and $x = x_L$, so the p_∞-related term can be written as

$$\int_{x_0}^{x_L} \left(\frac{p_\infty}{\rho} \frac{\partial \eta}{\partial x} \right) dx = \frac{p_\infty(x_L)}{\rho} \eta(x_L) - \frac{p_\infty(x_0)}{\rho} \eta(x_0) + \frac{\partial u_\infty}{\partial t} \int_{x_0}^{x_L} \eta dx = 0. \tag{20}$$

Since the rippled bed in the WCS is evolved from a flat sandy bed that is flush with the solid bed at x_0 and x_L, the integral of η from x_L to x_0 is zero (conservation of sand volume). As a result, the p_∞-related term is zero for both flat-bed and rippled-bed conditions, so our methodology automatically excludes the inertial-related pressure force. τ_b measured with equation (18) is the one defined in equation (7).

2.3. Experimental instrumentation

Since the flow condition from x_0 to the inside of the piston-end riser does not change with the bottom condition in the test section, it is reasonable to assume that Δp in equation (18) can be obtained by measuring the change of water pressure within the piston-end riser. Three OMEGA PX409 gauge pressure transducers were installed at three representative locations near the bottom of the piston-end riser, as shown in figure 2b and c. The measurement range is $0 \sim 1.0 \cdot 10^5$ Pa for units 2 and 3, and is $0 \sim 3.0 \cdot 10^4$ Pa for unit 1 (this unit is slightly different from the other two). The instrumentation error for all units is 0.03% of the measurement range, which translates to about 30 Pa for units 2 and 3, and

10 Pa for unit 1. Using a NI-DAQ board (National Instrument Data Acquisition Board) and LabView program, the measurements of gauge pressure and piston displacement are synchronized.

To measure the geometry of ripples within the WCS, a Laser-based Bottom Profiler (LBP) is adopted in this study. Two continuous laser lines in the longitudinal direction are projected on the movable bed, which are located 1/4 channel width (10 cm) on both sides of the channel's longitudinal centerline. Six side-viewing digital cameras capture these red laser lines in a dark environment, so a longitudinal bottom profile can be extracted from digital photos. The system's inaccuracy is estimated to be only 0.1 mm. Readers are referred to *Yuan et al.* [2017] for more information about the LBP system.

In some tests, a 2D Particle Image Velocimetry (PIV) system is used to measure the Reynolds-averaged flow field around one vortex ripple. Readers are referred to *Yuan and Madsen* [2014] for more details about the system setup. In this study, a 4M-pixel camera with a sampling frequency of 5.12 Hz is used, which gives a spatial resolution of about 1.5∼2 mm in both vertical and horizontal directions. Following *van der Werf et al.* [2007], the suspended sediment grains are simply used as seeding particles. The measurement window is about 30-40 cm long in both directions, which is sufficient to cover a half ripple from crest to trough in the horizontal direction and to reach a vertical elevation that is about 2∼3 ripple heights above the ripple crest. Since both flow condition and ripple shape are symmetric, the flow field above the other half ripple can be obtained by mirroring the measured half as follows. As an illustration, we consider point P1(x, z) in figure 1, where measured velocity $(u(t), w(t))$ is available. Point P2 is the mirror image of P1, such that $x_m = 2x - x_c$ and $z_m = z$, where x_c is the x-coordinate of the ripple crest.

The velocity at P2 is obtained as

$$\begin{cases} u_m = -u(t + T/2) \\ w_m = w(t + T/2) \end{cases} \tag{21}$$

In this way, the flow field over a whole vortex ripple can be obtained. The ripple profile is obtained by the LBP system. Note that the profile is measured after stopping the experiments, so it should be interpreted as a period-averaged ripple profile. However, during an experiment, the profile keeps deforming within a flow period, especially for the region around ripple crest. For simplicity, we treat the bottom as a stationary boundary following the LBP-measured ripple profile. As a result, the measurements in the very near-bottom region (a few milimeters from the ripple surface) are questionable. In this study, the PIV measurements are used to (1) confirm the obtained total bottom shear stress based on pressure measurements and (2) qualitatively illustrate coherent vortex motions at a few representative phases within a flow period. For these two objectives, the problem associated with a mobile ripple profile is not significant.

2.4. Experimental conditions

In this study, we only consider sinusoidal oscillatory flows. A total of 11 flow conditions cover flow period (T) from 6.25 to 10 s, free-stream velocity amplitude (U_∞) from 0.3 to 1 m/s and excursion amplitude, $A_b = U_\infty/\omega$, from 0.3 to 1 m. The Reynolds number $Re_w = U_\infty A_b/\nu$ is of the order 10^5 (even reaches 10^6), so our tests correspond to full-scale simulation of wave-driven near-bed flows. This differentiates the present study from many previous ones, which have much lower Re_w. For these flow conditions, vortex ripples are generated from an initially flat movable bed made of coarse sand with a median diameter of $d_{50} = 0.51$ mm. Ripple generation usually takes a few hundreds to thousands periods.

We closely monitored the ripple development and stopped the experiment when there was no visually detectable change of ripple shape within the last dozens or hundreds of periods. This ensures that equilibrium ripples were obtained in all tests. The test duration (from flat bottom to equilibrium ripples) is reported in table 1. For all tests ,the 9 m-long test section is mostly covered by very uniform 2D ripples, except for the near-end regions. Depending on the ripple size, the number of ripples in a ripple train is between 7 and 21 (see table 1). For example, figure 3 presents the LBP measurement of the rippled bed under test Ta040 (figure 3a), as well as a side-viewing photo (figure 3b) of the obtained equilibrium ripples. The periodic ripple profiles are ensemble-averaged into one representative ripple (figure 3c) with a height, H_R (vertical distance from crest to trough), and a length, λ (horizontal distance between two crests). The values are presented together with flow conditions in table 1. Due to the homogeneity of the ripple profiles, the variations of H_R and λ among individual ripples are generally about 1-10% of the mean values. The ripple shape is very symmetric with respect to the ripple's crest, as can be expected. Our measurements of H_R and λ are mostly within $10-20\%$ from the empirical predictor proposed by *O'Donoghue et al.* [2006], which is calibrated based on full-scale equilibrium ripples. This demonstrates that our tests indeed reached equilibrium conditions. Following *Madsen* [1993], a Shields parameter, ψ_{wmd}, which corresponds to the maximum wave bottom shear stress based on single-grain roughness $k_N = d_{50}$, is calculated to represent the intensity of flow condition, i.e.

$$\psi_{wmd} = \frac{\tau_{wmd}}{\rho(s-1)gd_{50}} = \frac{f_{wmd}{U_\infty}^2}{2(s-1)gd_{50}} \tag{22}$$

where $s = 2.65$ is the specific density of the sand, g is gravitational acceleration and f_{wmd} is a wave friction factor predicted using $k_N = d_{50}$ and the formula proposed by *Humbyrd*

[2012], i.e.

$$f_{wmd} = \exp\left[5.70\left(\frac{A_b}{k_N}\right)^{-0.101} - 7.46\right], 10 < \frac{A_b}{k_N} < 10^5. \quad (23)$$

Our tests cover ψ_{wmd} from 0.064, which is slightly higher than the critical value for incipient motion (ψ_{cr}=0.032), to 0.506, which is fairly close to the sheet-flow limit ($\psi_{wmd} = 0.7$) proposed by *Madsen* [1993].

Once the equilibrium sand ripples were developed, the water pressure measurements from the three pressure transducers were collected for 20-30 periods. The corresponding flat-bed measurements were obtained by running the same flow condition over a fixed rough bed covered by sandpaper. This fixed bed was used by *Yuan and Madsen* [2014, 2015] for studying wave and wave-current boundary layer flows, and its equivalent Nikuradse sand-grain roughness, $k_N = 3.7$ mm, has been carefully determined in previous experiments. This k_N will be used for estimating the skin bottom shear stress $\tau_{b,f}$ in equation (18). In two tests, Ta040 and Ta060, PIV measurements were obtained to validate and interpret the measurements of total bottom shear stress.

3. Data analysis

For each measurement, there is one record of piston displacement and three records of water pressure (from three transducers). Our measurements suggest that the discrepancy between the three transducers is of O(10 Pa), which agrees with the instrumentation accuracy. Therefore, the three synchronized pressure records are first averaged into one record.

The first step of data analysis is to ensemble-average the measurements, i.e.

$$< \xi(t) >= \frac{1}{N_P}\sum_{n=1}^{N_P} \xi(t + (n-1)T) \quad (24)$$

where N_p (usually about 20-30) is the number of periods, and ξ is either piston displacement S or water pressure p. For brevity, the ensemble-averaging operator "<>" will be neglected hereafter. The obtained ensemble average is subsequently converted to Fourier series, i.e.

$$S(t) = \sum_{n=1}^{\infty} S_n \cos(n\omega t + \varphi_{sn}) \tag{25}$$

and

$$p(t) = \sum_{n=1}^{\infty} p_n \cos(n\omega t + \varphi_{pn}) \tag{26}$$

where S_n and p_n are the n-th-harmonic amplitudes, and φ_{sn} and φ_{pn} are the n-th-harmonic phases. To synchronize a pair of tests with different bottom conditions, the time coordinate, t, is adjusted to make the first-harmonic phase of piston displacement equal to $-\pi/2$, i.e., $\varphi_{s1} = -\pi/2$. By doing so, the first-harmonic free-stream velocity follows equation (1). The pressure difference between rippled- and flat-bed tests can be straightforwardly calculated and converted to a Fourier series

$$\Delta p = p_r(t) - p_f(t) = \mathrm{Re} \sum_{n=1}^{\infty} \Delta p^{(n)} e^{in\omega t} \tag{27}$$

where the subscripts r and f indicate rippled and flat beds, respectively, and the n-harmonic complex amplitude $\Delta p^{(n)}$ is

$$\Delta p^{(n)} = \Delta p_n \cos(\varphi_{\Delta pn}) \tag{28}$$

with Δp_n and $\varphi_{\Delta pn}$ being the amplitude and the phase, respectively.

It is found that the vibration of test section's glass sidewall around the natural frequency (about 1Hz) of the facility controls the obtained pressure difference. Also, the actual oscillatory flows between a pair of tests were not perfectly identical. Therefore, some data

corrections were employed to filter out these minor effects, as described in Appendix A. In summary, the raw pressure difference is corrected in three steps: (a) remove Fourier components higher than the 5th harmonic, which are due to sidewall vibration, (b) correct for imperfect flow generation and (c) remove the even (2nd and 4th) harmonics, which are unrealistic for sinusoidal oscillatory flows. The obtained Δp is subsequently used in calculating total bottom shear stress, $\tau_b(t)$, via equation (18). To facilitate the comparison among tests, $\tau_b(t)$ is converted to a time-varying friction factor f_τ and expressed as a Fourier series

$$f_\tau(t) = \frac{2\tau_b}{\rho {U_\infty}^2} = \mathrm{Re}\left(\sum_{n=1,3,5} f^{(n)} e^{in\omega t}\right) = \sum_{n=1,3,5} f_n \cos(n\omega t + \phi_{fn}) \tag{29}$$

where $f^{(n)}$ is the complex amplitude of the n-th harmonic with f_n and ϕ_{fn} being the amplitude and the phase, respectively. Here f_τ, following the corrected Δp, only contains 1st, 3rd and 5th harmonics.

The experimental error for each harmonic of f_τ is estimated based on the error for Δp as follows. In our experiments, each pressure record contains N_p =20-30 periods, so we can Fourier analyze the measured pressure period-by-period, and calculate the standard deviation $\sigma_{p,n}$ for n-th Fourier component among these N_p periods, i.e.

$$\sigma_{p,n} = \sqrt{\frac{\sum_{i=1}^{N_p} \left({p_i}^{(n)} - p^{(n)}\right)^2}{N_p - 1}} \tag{30}$$

where ${p_i}^{(n)}$ is the complex amplitude of n-th harmonic pressure for the i-th flow period in a continuous pressure record, and $p^{(n)}$ is the n-th-harmonic component of the ensemble-averaged pressure, i.e. defined in equation (26). The 95% confidence limit of $p^{(n)}$ is

$$\varepsilon_{p,n} = \frac{1.96\sigma_{p,n}}{\sqrt{N_p - 1}}. \tag{31}$$

For a pair of tests, the experimental error can be considered independent, so the 95% confidence limit of n-th-harmonic pressure difference, $\Delta p^{(n)}$ defined in equation (28), is

$$\varepsilon_{\Delta p,n} = \sqrt{{\varepsilon_{p,n,r}}^2 + {\varepsilon_{p,n,f}}^2} \tag{32}$$

where the subscripts r and f indicate the rippled- and flat-bed tests, respectively. We take $\varepsilon_{\Delta p,n}$ as the uncertainty for $\Delta p^{(n)}$. Following equations (18) and (29), the uncertainty for f_n (the amplitude of $f^{(n)}$) is

$$\varepsilon_{fn} = \left(\frac{2h}{\rho L {U_\infty}^2}\right) \varepsilon_{\Delta p,n}. \tag{33}$$

Assuming that the experiment error for $f^{(n)}$ can have any phase angle, adding such an error to $f^{(n)}$ will change the phase angle, ϕ_{fn}, of $f^{(n)}$. If $\varepsilon_{fn} < f_n$, the maximum change of ϕ_{fn} occurs when the error and $f^{(n)}$ are 90° out of phase, so

$$\Delta\phi_{fn} = \tan^{-1}\left(\frac{\varepsilon_{fn}}{f_n}\right). \tag{34}$$

We simply take $\Delta\phi_{fn}$ as the 95% confidence limit for ϕ_{fn}. If $\varepsilon_{fn} > f_n$, the experimental error is larger than the measurement in amplitude, so ϕ_{fn} can be changed to any value by adding the error. This situation only occurs for the 3rd and the 5th harmonics of f_τ, which can be very small in amplitude.

4. Experimental Results

In this section, the experimental results are presented based on the friction factor f_τ. We first discuss the three Fourier components (1st, 3rd and 5th), and then present the intra-period variation.

4.1. Fourier components of total bottom shear stress

Table 2 summarizes the amplitudes and the phases for the leading three odd harmonics of f_τ. The relative experimental error for the amplitude is defined as

$$\Delta f_n = \frac{\varepsilon_{f_n}}{f_n}, n = 1, 3, 5 \tag{35}$$

Generally speaking, the first-harmonic, $f^{(1)}$, is the dominant one. Its amplitude is mostly between 0.1-0.2, which is one order of magnitude larger than the other two harmonics. Also, its uncertainty is very small (Δf_1 is less than 10%), except for Test Td057 (11.3%), and $\Delta\phi_{f1}$ is only a few degrees. This is because the first-harmonic pressure difference, $\Delta p^{(1)}$, is about 200-500 Pa in amplitude, which is much larger than its experimental error $\varepsilon_{\Delta p,1}$ (of O(10) Pa) estimated with equation (32). $f^{(3)}$ and $f^{(5)}$ are considerably smaller, but their absolute experimental error is comparable to that of $f^{(1)}$, so the relative error is much larger, e.g., even above 100% for some tests.

For wave boundary layer over a flat bottom, f_τ depends on the relative roughness A_b/k_N [e.g., *Yuan and Madsen*, 2014]. Many predictive models [e.g., *Grant and Madsen*, 1982] assume that k_N for vortex ripples is scaled with the ripple height H_R, but the difference among various predictive models is quite significant. We shall specifically discuss this later, so here we simply choose A_b/H_R as an indicator of relative roughness, and study how this parameter affects the Fourier components of f_τ. It is of interest to compare our tests with those conducted by *Lofquist* [1980], who also measured the intra-period variation of total bottom shear stress for ripples developed with coarse sand ($d_{50} = 0.55$ mm). We re-analyzed the time series of total bottom shear stress for six of Lofquist's tests (tests 1, 2, 3, 13, 18, 24), which have equilibrium 2D ripples, to obtain the first-harmonic

friction factor $f^{(1)}$. Higher order harmonics are not included, as they may not be reliable due to high experimental error.

The first harmonic is presented in figure 4. The Shields parameter ψ_{wmd} is indicated by the marker's color. It can be observed that A_b/H_R increases with ψ_{wmd}, i.e. $A_b/H_R \sim 3$ for $\psi_{wmd} < 0.1$ and $A_b/H_R \sim 8$, for $\psi_{wmd} \sim 0.45$. The six points from *Lofquist* [1980] have smaller A_b/H_R than our tests, which is primarily because these tests have lower Shields parameter (ψ_{wmd} is less or close to 0.1) than ours (from 0.064 to 0.48). Nevertheless, the two datasets nicely form continuous variations for both f_1 (amplitude) and ϕ_{f1} (phase). Generally speaking, f_1 decreases with A_b/H_R, i.e., from $f_1 \sim 0.25$ for $A_b/H_R \sim 3$ to $f_1 \sim 0.10$ for $A_b/H_R \sim 8$. Since the ripples are washed-off by increasing ψ_{wmd}, f_1 should decrease towards the value for sheet-flow conditions, which is of O(0.01). Therefore, the observed decreasing trend primarily reflects the washing-off effect associated with higher ψ_{wmd}. The data scatter is relatively larger for ϕ_{f1}, but it can still be commented that ϕ_{f1} decreases with A_b/H_R from about 20° for $A_b/H_R \sim 3$ to -20° for $A_b/H_R \sim 6$. This indicates that the first-harmonic total bottom shear stress is generally in phase with the free-stream velocity or even lag behind in phase. Most wave boundary layer models developed for flat rough bed, however, would predict a phase lead close to 45° for very large bottom roughness (small A_b/k_N).

The third and the fifth harmonics have quite large (over 10%) experimental error. Only for six tests, which are marked by adding "(s)" to the test ID in table 2, the relative error Δf_3 and Δf_5 are both less than 50%, so only these results are shown in figure 5. The third-harmonic amplitude, f_3 (figure 5a), is generally around 0.02, and no significant dependency on A_b/H_R can be observed, due to the large experimental error. The third-

harmonic phase, ϕ_{f3} (Figure 5b), is generally within $-110°$ to $-140°$, and there is also no significant dependency on A_b/H_R. For flat-bed scenarios, *Yuan and Madsen* [2014] showed that $f_3 \approx 0.14 f_1$ and $\phi_{f3} \approx 3\phi_{f1}$. For the six selected tests, f_3 is about 13% of f_1 on average, which agrees with the flat-bed results, but ϕ_{f3} deviates a lot from $3\phi_{f1}$ ($\sim -60°$ to $60°$). For the fifth harmonic, the high uncertainty again prevents concluding any significant dependency on A_b/H_R. The amplitude f_5 (figure 5c) is about 0.02 to 0.04, and the phase ϕ_{f5} (figure 5d) is generally within 0 to $-50°$, except for two points (around $-70°$) for the two tests with longer period (Tc060 and Tc75). The fifth harmonic should be almost zero for flat-bed scenarios, but it is comparable to or larger than the third-harmonic for our ripple-bed tests. This, together with the fact that ϕ_{f1} and ϕ_{f3} do not agree with those for flat-bed scenarios, indicate that the intra-period variation of f_τ for a ripple bed may be significantly different from that for a flat bed. The generally accepted $\tau_b \sim \cos(\omega t)$ or $\tau_b \sim |\cos(\omega t)|\cos(\omega t)$ cannot well approximate bottom shear stress for rippled-bed conditions. This will be further illustrated in the next sub-section.

4.2. Intra-period variation of total bottom shear stress

Among all 11 of our tests, 6 tests have reliable measurements of all three harmonics of f_τ (relative error for amplitude is less than 50%), so intra-period variations f_τ of these tests are presented in figure 6. Since the first-harmonic $f^{(1)}$ is the dominant Fourier component, and it is almost in phase with the $u_\infty(t)$, f_τ is generally in-phase with $u_\infty(t)$. f_τ is mostly due to the form-drag component, i.e., the first term on the right-hand side of equation (18), so it can be concluded that the form drag is almost in-phase with free-stream velocity. Adding the higher-order harmonics, especially the fifth harmonic, makes the time series of f_τ quite wavy with multiple local peaks. Although our measurements

of $f^{(3)}$ and $f^{(5)}$ are not very accurate, it can still be observed that three peaks within one half-period occur at more-or-less the same phases for the six shown tests. As highlighted by red crosses for test Ta060 in figure 6, there is one primary peak slightly after $\theta = 0°$ (P1), and two secondary peaks around $\theta = 60°$ (P2) and $\theta = 110°$ (P3). Comparing Ta-series tests ($T = 6.25$ s, top two rows of figure 6) with Tc-series tests ($T = 8.33$ s, bottom row of figure 6), the secondary peaks become less significant for longer-period tests. For flat-bed conditions, there should only be one primary peak for each half period, which leads the maximum free-stream velocity in phase [e.g., *Jensen et al.*, 1989]. Thus, the intra-period variation of total bottom shear stress for flat- and ripple-bed conditions are very different.

As a verification of these pressure-based results, an alternative approach based on flow measurements is applied to some tests. In this approach, the total flow resistance can be estimated from velocity fields through a control-volume analysis. As shown in figure 1, a control volume (the region enclosed by the red dashed line), which covers the flow field between two adjacent ripple troughs, is considered in the following discussion. The bottom of the control volume follows the ripple surface, while the top of the control volume is within the free-stream region. The rate of change of momentum within the control volume is related to the total force and the total momentum flux through the control volume's boundary. Here we only consider the momentum in the horizontal direction. Due to periodicity of the flow field in x-direction, the momentum fluxes through the two lateral boundaries cancel each other. There is also no momentum flux through the top (local velocity is parallel to the boundary) and the bottom (assuming an impermeable bed). If the origin of the $x - z$ coordinate is set at the left-side ripple trough, the control-volume

analysis gives

$$\frac{\partial M}{\partial t} = \frac{\partial}{\partial t}\int\limits_{CV} \rho u dA = \int\limits_0^h p(0,z)dz - \int\limits_0^h p(\lambda,z)dz + \rho F_b \tag{36}$$

where M is the momentum within the control volume, $p(0,z)$ and $p(\lambda,z)$ are water pressure along the lateral boundaries $x = 0$ and $x = \lambda$, respectively, and F_b is the total force from the bed. Following equation (3) water pressure can be split into a free-stream component, p_∞, which satisfies equation (4), and a local component p', which is periodic in x. Thus, equation (36) can be re-written as

$$F_b = \frac{\partial}{\partial t}\int\limits_{CV} u dA - \int\limits_0^h \left[p_\infty(0,z) - p_\infty(\lambda,z)\right]/\rho dz = \frac{\partial}{\partial t}\int\limits_{CV} u dA - h\lambda\frac{\partial u_\infty}{\partial t}. \tag{37}$$

We can define that $u = 0$ within the vortex ripple, so equation (37) can be written as

$$F_b = \int_0^\lambda \frac{\partial}{\partial t}\left[\int_0^h (u - u_\infty)\, dz\right] dx. \tag{38}$$

Due to conservation of mass, the vertical integral in the bracket in equation (38) is not a function of x, so

$$\frac{F_b}{\lambda} = \frac{\partial}{\partial t}\left[\int_0^h (u - u_\infty)\, dz\right]. \tag{39}$$

The total force F_b from the bottom includes the inertial force F_I related to p_∞, i.e., equation (5) , so the total bottom shear stress is obtained after removing it from F_b, i.e.

$$\tau_b = \frac{F_b - F_I}{\lambda} = \frac{\partial}{\partial t}\left[\int_0^h (u - u_\infty)\, dz\right] - \frac{\partial u_\infty}{\partial t}\frac{V_{ripple}}{\lambda} \tag{40}$$

where V_{ripple} is the volume of ripple above its trough, which is given by the LBP measurement. Equation (40) suggests that τ_b can be estimated by measuring the velocity profile at the ripple trough. This provides another approach for measuring τ_b, which can be used to validate the pressure-based technique.

In this study, PIV measurements of the flow field are obtained for two tests, Ta040 and Ta060 ($T = 6.25$ s, see table 1 for other details). For these tests, the flow is sampled at a frequency $f = 5.12$ Hz (32 samples per flow period) continuously for 32 periods, so the velocity measurements can be phase-averaged. The upper limit of the measurement window is about 2∼3 ripple heights above the ripple crest. Local measurements confirm that the flow near the upper limit is within the free-stream region, so the PIV results can be used to estimate τ_b via equation (40). The time derivative is calculated using central difference. Due to the relatively low sampling frequency, the obtained τ_b is quite noisy, so it is filtered by only keeping the leading three odd harmonics (1st, 3rd and 5th harmonics). Figure 7 compares the estimates of τ_b from the two approaches. PIV-based results generally agree well with the pressure-based results for test Ta040. However, for Ta060 the PIV-based result contains a significant fifth harmonic with an amplitude comparable to the first harmonic, so it appears very wavy and is out of phase with the pressure-based method results. The higher-order harmonics for the PIV-based results are not expected to be reliable, because the PIV measurements have a low frequency (5.12 Hz) that cannot accurately resolve the higher-order harmonics, e.g. the 5.12 Hz is only about 6 times the frequency of the fifth harmonic (0.8 Hz) of the two selected tests. Also, the phase-averaging only involves 32 ensembles, so some residual turbulence still remains in the free-stream velocity u_∞, which may affect the results. Therefore, here we only compare the results for the first-harmonic τ_b. As shown in table 3, the first-harmonic amplitude ,f_1, from the PIV approach is $\sim 20\%$ smaller than that from the pressure approach, and the difference between the first-harmonic phase is only $\sim 10°$. For flat-bed conditions, *Yuan and Madsen* [2014] pointed out that bottom shear stress estimated via a momentum-

integral approach (similar to our PIV approach) suffers from some secondary circulation in the transverse plane of the test section, and therefore underestimates the bottom shear stress. It seems that such an effect may also exist for our ripple-bed condition, which explains why the PIV approach gives smaller f_1. The ripple profile and the flow field are not perfectly periodic in x-direction, which is another possible source of inaccuracy. Nevertheless, the agreement between the two approaches can still be considered good, which verifies our pressure-based measurement technique.

The multiple peaks of total bottom shear stress is possibly because of the coherent vortex motion. To demonstrate this, the vorticity component perpendicular to the measurement plane is obtained based on the phase-averaged velocity via

$$\omega_y = \frac{\partial u}{\partial z} - \frac{\partial w}{\partial x} \tag{41}$$

where u and w are horizontal and vertical components of phase-averaged velocity. ω_y is further normalized as $\omega_y^* = T\omega_y/2\pi$. Figure 8 presents the PIV measurements for three phases from test Ta060, which are close to the phases P1 to P3 identified in figure 6. The colored shades indicate ω_y^* and the vectors indicate the phase-averaged velocity. The phase $\theta = 7.093°$ is close to the primary peak P1. At this phase, the free-stream velocity just passed its maximum value, and flow separation at the ripple crest produces a coherent vortex in the lee side, which is closely attached to the ripple surface. It can be expected that water pressure is low within the lee vortex, so the pressure difference between the two ripple flanks produces a large horizontal net pressure force. The flow deceleration leads to an unfavorable pressure gradient that can enhance flow separation and vortex development, so the primary peak (P1) can occur after the maximum free-stream velocity ($\theta = 0°$). From P1 ($\theta \sim 10°$) to P2 ($\theta \sim 60°$), the vorticity within the lee vortex reduces,

e.g. for $\theta = 63.3°$ the blue color associated with the lee vortex becomes lighter. One key feature around the phase of P2 is that the lee vortex starts to detach from the ripple, i.e. the blue cloud starts to move upward, so the secondary peak of total bottom shear stress at P2 is possibly linked to the vortex detachment. From P2 to P3, the free-stream velocity changes direction, and the detached coherent vortex is convected over the ripple crest to the other (left-hand) side of the ripple crest. The PIV measurements at $\theta = 119.6°$ suggest that the detached vortex is just above the ripple crest at this phase (the area above ripple crest is light blue). Under its influence, the flow near the ripple crest is significantly enhanced and much stronger than the free-stream value, and a new coherent vortex starts to develop on the other (left-hand) side of the ripple crest. Although it is impossible to confirm the actual water pressure near the ripple surface from PIV measurements, the fact that the three multiple peaks occur at three critical moments of vortex development indicate that they are closely related to coherent vortex motion. More research effort, e.g., direct measurement of water pressure at ripple surface or high-fidelity numerical modeling, is required to further improve our understanding on this phenomenon.

5. Equivalent sand-grain roughness for equilibrium ripples

Over the past decades, many wave friction factor formulas have been developed, which require the equivalent sand-grain roughness, k_N, as a model input to predict bottom shear stress τ_b. For small roughness, e.g., a flat sandy bed, k_N controls the logarithmic velocity distribution within the very near-bed region of a wave boundary layer, so it can be directly estimated from velocity measurements. However, for ripple-bed conditions the near-bed logarithmic layer vanishes due to the large physical bottom roughness, so k_N is no longer a well-defined physical quantity, but becomes a model parameter. It depends

on which formula is adopted for predicting τ_b and/or other boundary layer physics. Very few direct measurements of τ_b are available, so k_N is usually determined based on energy dissipation rate $\dot{E}_d$, which can be estimated e.g., from wave height attenuation. An immediate question is whether the obtained k_N can indeed give good prediction of τ_b. In this section, we attempt to address this question with our direction measurements of τ_b. A new predictor of k_N is also calibrated based on our measurements.

5.1. On determining k_N from wave energy dissipation

Kajiura [1968] showed that $\dot{E}_d$ is related to τ_b through

$$\dot{E}_d = \overline{\tau_b u_\infty}. \tag{42}$$

Two possible temporal variations of τ_b are commonly assumed in previous studies, i.e.

$$\tau_b(t) = \begin{cases} \tau_{bm}\cos(\omega t + \varphi_{\tau bm}) \\ \tau_{bm}|\cos(\omega t + \varphi_{\tau bm})|\cos(\omega t + \varphi_{\tau bm}) \end{cases} \tag{43}$$

where τ_{bm} and $\varphi_{\tau bm}$ are the amplitude and the phase lead of maximum bottom shear stress. Conventionally, τ_{bm} is expressed in terms of a wave friction factor f_w as

$$\tau_{bm} = \frac{1}{2} f_w \rho {U_\infty}^2. \tag{44}$$

Equations (43) and (1) together give $\dot{E}_d$. Some researchers neglect $\varphi_{\tau bm}$, so the normalized energy dissipation rate $\dot{E}_d^* = \dot{E}_d/(\rho U_\infty^3)$, depending on which temporal variation in Equation (43) is adopted, has four possible options. Consequently, the friction factor (denoted as f_w' here) inferred from $\dot{E}_d^*$ also has four options

$$f_w' = \left\{ \begin{array}{c} 4\dot{E}_d^* \\ \frac{3\pi}{2}\dot{E}_d^* \\ \frac{4}{\varphi_{\tau bm}}\dot{E}_d^* \\ \frac{3\pi}{2\varphi_{\tau bm}}\dot{E}_d^* \end{array} \right\} \tag{45}$$

The first two options neglect $\varphi_{\tau bm}$. A friction factor formula usually predicts f_w (and $\varphi_{\tau bm}$) with the information of A_b/k_N, so k_N can be back-calculated with f_w' and a wave friction factor formula. This is the methodology of many previous studies. However, we have shown that the temporal variation of τ_b for oscillatory flow over vortex ripples cannot be well approximated by neither of the two options in equation (43), so the inferred f_w' may not be the actual f_w that represents the maximum bottom shear stress. As a result, all previous studies that adopted the methodology outlined here may not have accurate estimates of f_w. The obtained k_N predictor, although is guaranteed to yield accurate prediction of $\dot{E}_d$, cannot lead to accurate prediction of f_w. It is worthwhile to check this issue with the direct measurement of f_w,.

The experimental value of $\dot{E}_d^*$ for our tests can be obtained through (note that u_∞ only has a first harmonic)

$$\dot{E}_d^* = \frac{1}{4}\left(f_1 \cos\varphi_{f1}\right) = \frac{1}{4}\left(\frac{f_1}{f_w} f_w \cos\varphi_{f1}\right). \tag{46}$$

Comparing equations (45) and (46), the ratio f_w'/f_w is

$$\frac{f_w{}'}{f_w} = \left\{ \begin{array}{c} \frac{f_1}{f_w}\cos\varphi_{f1} \\ \frac{3\pi}{8}\frac{f_1}{f_w}\cos\varphi_{f1} \\ \frac{f_1}{f_w}\frac{\cos\varphi_{f1}}{\cos\varphi_{\tau bm}} \\ \frac{3\pi}{8}\frac{f_1}{f_w}\frac{\cos\varphi_{f1}}{\cos\varphi_{\tau bm}} \end{array} \right\}. \tag{47}$$

This ratio depends on the value f_1/f_w, and f_w is just the peak value of f_τ shown in figure 6. Figure 9 compares the measured f_w and f_1. Although f_w is slightly larger than f_1, a straight line fitted to the data points (the black dashed line), which is through the origin, has a slope of 1.095, indicating that f_w is only about 10% larger than f_1 on average. Thus, we can approximately take that f_1/f_w=1/1.095. The measurements of φ_{f1} is generally within $\pm 20°$, so $\cos\varphi_{f1}$ is generally within 0.94∼1, and we can take 0.97 as an average. This suggests that $f'_w/f_w = 0.89$ and 1.04 for the first two options in equation (45), respectively. For many friction factor formulas, the associated $\varphi_{\tau bm}$ predictor gives fairly large $\varphi_{\tau bm}$ for very large bottom roughness ($A_b/k_N \sim 1$), e.g., $\varphi_{\tau bm}$ approaches 45° in the models of *Humbyrd* [2012]. If we take $\varphi_{\tau bm} \approx 45°$, f'_w/f_w is 1.25 and 1.48 for the third and the fourth options in equation (45), respectively. Obviously, option 2, which neglects $\varphi_{\tau bm}$ and assumes that $\tau_b \sim \cos(\omega t)|\cos(\omega t)|$ is the best option for estimating f_w from measured energy dissipation rate, since it merely overestimates f_w by 4%. Any k_N predictor that is developed based on this option, e.g. ,*Wikramanayake and Madsen* [1994], *Nielsen* [1983] and *Grant and Madsen* [1982], can yield accurate prediction for both wave friction factor (or maximum bottom shear stress) and energy dissipation rate, if the predictor is used together with the corresponding wave friction factor formula. Otherwise, the predictor is only applicable for prediction energy dissipation rate. This conclusion does not imply that $\tau_b \sim \cos(\omega t)|\cos(\omega t)|$ is the true temporal variation. It should be interpreted as that this temporal variation happens to give the same (or very closely the same) energy dissipation rate as the actual τ_b for ripple-bed conditions.

5.2. A new predictor for k_N

Instead of calibrating k_N based on $\dot{E}_d^*$, we can directly calibrate a k_N-predictor based on our measurements of wave friction factor f_w. To this end, we select the model proposed by *Humbyrd* [2012]. This model analytically predicts f_w, which is approximated by explicit formula with A_b/k_N as the only model parameter. For large bottom roughness, the explicit formula is

$$f_w = \begin{cases} 2\left(\dfrac{30}{\kappa}\dfrac{A_b}{k_N}\right)^{-2/3}, 0.05 < \dfrac{A_b}{k_N} < 0.342 \\ \exp\left[-1.69\left(\dfrac{A_b}{k_N}\right)^{0.344} - 0.473\right] + 0.0388, 0.342 < \dfrac{A_b}{k_N} < 10 \end{cases} . \tag{48}$$

Experimental values for k_N are back-calculated with measured f_w and equation (48). We subsequently calculate the ratio, $\alpha_k = k_N/H_R$. The results suggest that α_k increases with the ripple steepness H_R/λ, so figure 10a plots α_k against H_R/λ. It should be noted that f_w is partially determined by the higher-order harmonics of bottom shear stress, which may suffer very significant experimental error. The six tests with reliable measurements of higher-order harmonics (the ones shown in figure 6) are highlighted as full circles in figure 10a. It can be seen that the tests with large error for higher-order harmonics also nicely follow the trend determined by the six selected tests, so the experimental error appears to have negligible influences. Generally speaking, α_k increases from about 4 to 10 for H_R/λ from 0.14 to 0.22. It should be noted that H_R/λ generally decreases with increasing Shields parameter ψ_{wmd} defined in equation (22), which is associated with the fact that ripples are washed-off by increasing ψ_{wmd}. Therefore, the results suggest that the bottom becomes relatively "smoother" as the ripples becomes increasingly washed-off. The majority of obtained α_k values are within 3 to 8, except for one test (α_k for Td044 is 9.67). Among the previous k_N predictors calibrated based on energy dissipation rate,

Wikramanayake and Madsen [1994] obtained $k_N = 4H_R$. They adopted a wave friction factor formula that is quite similar to the one used in this study. They also assumed $\tau_b \sim \cos(\omega t)|\cos(\omega t)|$ and neglected $\varphi_{\tau bm}$. Therefore, it is not surprising that their result is close to ours. The following formula is fitted to obtained $\alpha_k - H_R/\lambda$ relationship

$$\frac{k_N}{H_R} = \alpha_k = \begin{cases} 4, \frac{H_R}{\lambda} < c_0 \\ c_1(\frac{H_R}{\lambda} - c_0) + 4, \frac{H_R}{\lambda} \geq c_0 \end{cases} . \tag{49}$$

Here a lower limit c_0 for H_R/λ is imposed to avoid α_k becoming too small for very low value of H_R/λ. Since our measurements do not cover the region for low H_R/λ, we simply force $\alpha_k = 4$, following *Wikramanayake and Madsen* [1994]. The fitted parameters are $c_0 = 0.155$ and $c_1 = 68.6$, and the fitted α_k predictor is shown as the solid line in figure 10a. The average relative difference between the predictor and the measurements is 15%. Using this calibrated k_N predictor, the predictions of f_w are compared with the measurements in figure 10b. The prediction agrees well with the data, and the relative predictor-data discrepancy is only 7% on average. To further demonstrate the predictor's performance, it is applied to the six selected tests from *Lofquist* [1980], which are not used in the calibration. Except for one test (test 13), which has a questionably large $f_w = 0.45$, good prediction of f_w is also obtained with the new k_N predictor.

The merit of the proposed k_N predictor is that it can give reliable prediction of total bottom shear stress when used with the *Humbyrd* [2012]'s formula for friction factor. However, it should be pointed out that the dataset for calibration is limited to fully developed 2D ripples under periodic oscillatory flows. More future work is required to extend the dataset to non-equilibrium ripples (e.g. the transient stage before reaching equilibrium), 3D ripples and ripples under irregular oscillatory flows.

6. Conclusion

In this study, a pressure-based measurement technique was successfully developed for quantifying the total flow resistance (or total bottom shear stress τ_b) over rippled movable bed in an oscillatory water tunnel. This technique is based on the fact that the water pressure around the piston end of the facility increases with the total flow resistance within the test section. Thus, by comparing the measurements with a pair of tests, which have identical flow but different bottom conditions (flat and rippled beds), τ_b for a rippled bed can be measured. Experiments were conducted with sinusoidal oscillatory flows over a movable bed made of coarse sand, corresponding to full-scale simulations of near-bed wave-driven flows with Reynolds number up to $O(10^5 \sim 10^6)$. 2D equilibrium ripples were produced in all tests. The measured pressure difference was corrected by removing the influences of imperfect flow generation, facility resonance and unrealistic even-order harmonics, so only the leading three odd harmonics (1st, 3rd and 5th) are kept in the final measurement. PIV measurements were also obtained for two tests with the purpose of validating the pressure-based measurements and interpreting key features of the intra-period variation of total bottom shear stress.

Our experimental results suggest that the first harmonic is the dominant one among the leading three odd harmonics of τ_b. Its amplitude decreases with A_b/H_R, which increases with a characteristic Shields parameter ψ_{wmd}, suggesting that the form drag reduces as the ripples are washed-off by higher ψ_{wmd}. Its phase is generally within $\pm 20^\circ$ from that of the free-stream velocity, and also decreases with A_b/H_R, so total bottom shear stress is generally in-phase with the free-stream velocity. The third and the fifth harmonics suffer from quite large experimental error, which is only acceptable (relative error for amplitude

is less than 50%) for 6 of totally 11 tests. Based on limited measurements, the third harmonic is about 13% of the leading first harmonic, which agrees with the experimental results for flat rough bed. However, its phase is about $-110°$ to $-140°$ behind the free-stream velocity, which does not agree with the flat-bed conditions. The fifth harmonic is comparable to (or even larger than) the third harmonic, which is not true for flat-bed conditions.

Based on a control-volume analysis, it is shown that τ_b can be obtained by measuring the horizontal velocity above the ripple trough, which gives another experimental approach based on PIV measurement. The comparison between the PIV-based and the pressure-based approaches shows a reasonable agreement between the two. The PIV-based approach gives slightly smaller first harmonic of τ_b, which is possibly due to secondary flow in the transverse plane of the WCS. Nevertheless, the agreement can still be taken as a good validation for both approaches.

The intra-period variation of τ_b exhibits three peaks with one half period. The primary peak is just slightly after the maximum free-stream velocity u_∞, when a strong separation vortex is developed and attached to the lee-side ripple flank. Around 60° after maximum u_∞ (when the flow is still decelerating), one secondary peak can be observed in most time series of τ_b. PIV measurement suggests that the lee-side vortex is about to be detached from the ripple flank at this phase. The other secondary peak occurs about 110° after the maximum u_∞, when u_∞ has been reversed. Around this moment, the detached lee-side vortex has just passed the ripple crest, when it is convected to the other side of the ripple crest. These observations suggest that coherent vortex motion controls the intra-period variation of τ_b.

Our measurements suggest that the maximum wave bottom shear stress, τ_{bm}, (or the wave friction factor) can be best estimated from the energy dissipation rate, if the temporal variation of bottom shear stress is assumed to be $\sim \cos(\omega t)|\cos(\omega t)|$. Thus, previous studies, which adopted this temporal variation for calibrating predictors of equivalent sand-grain roughness, k_N, should be able to well predict τ_{bm} and energy dissipation rate. A new k_N predictor to be used with *Humbyrd* [2012]'s for wave friction factor is developed based on our experimental results of τ_{bm}.

It is found that k_N is about 3-10 times the ripple height, and k_N increases with the ripple steepness. The merit of this predictor is that it is established directly with high-quality full-scale measurement of total bottom shear stress under oscillatory flows over equilibrium ripples. However, to make it applicable for field conditions, future work is required to extend the dataset for non-equilibrium ripples, 3D ripples and irregular oscillatory flows.

Appendix A: Correction for pressure difference

The raw pressure difference calculated with equation (27) is contaminated by the vibration of the test section's sidewall and the imperfect flow generation. This appendix provides some evidences for these minor effects. Data correction methods are also introduced. To facilitate the presentation, the following introduction will be based on one representative test, Ta040 (U_∞=0.4 m/s, T=6.25 s).

Figure A1 shows the obtained water pressure $p(t)$ and its amplitude spectrum (frequency is normalized by the primary flow frequency $f_1 = 2\pi/T$) for both flat and rippled-bed conditions of test Ta040. Since most of the water pressure is required to drive the oscillatory flow, $p(t)$ and $u_\infty(t)$ are roughly 180° out of phase. It can be clearly seen that

some high-frequency harmonics with quite significant amplitudes exist, making the time series of $p(t)$ quite wavy. From the amplitude spectra (Figure A1b,c), there are some significant harmonics with normalized frequencies around 7-10 (absolute frequency about 1-1.5 Hz). We believe that they are produced by the vibration of test section's sidewall. In some tests, we measured the sidewall vibration using a few Linear Variable Displacement Transformers (LVDT) with a measuring scope of 5 mm. The sensors were located at the centroids of the sidewalls. The measured time series of sidewall displacement (of the order 0.1 mm) are converted into energy spectra. It is found that most of the spectral energy is concentrated around 1-1.5 Hz, regardless of the primary frequency of the oscillatory flow in the test section. Since our test section is 9 m-long, a small sidewall vibration will displace a non-negligible amount of water, which is equivalent to adding another piston to the system. Consequently, an additional high-frequency water pressure is produced.

Figure A2a shows the pressure difference Δp for Test Ta040. It can be seen that some high-frequency harmonics associated with the sidewall vibration around f=1 Hz control the obtained Δp. From the amplitude spectrum of Δp shown in figure A2c, 7th-9th harmonics (amplitudes from 700-1100 Pa) are much larger than the first harmonic ($\sim$200 Pa). This is because the sidewall vibration is not very repeatable, so the corresponding water pressure changes significantly between a pair of tests. The Δp related to boundary layer flows should be concentrated around the flow's primary frequency ($1/T$ $\sim$0.1 to 0.16 Hz) in the frequency spectrum, which is quite separated from the $\sim$ 1 Hz region. Thus, it is reasonable to believe that the sidewall vibration does not interfere with the key boundary layer physics of interests, and we can simply filter out the high-frequency Δp. For the shortest flow period in our tests, i.e. 6.25 s, the fifth harmonic ($f_5 = 0.8$ Hz)

is close to the 1 Hz region controlled by sidewall vibration, so the Fourier components with frequency higher than five times the primary harmonics is filtered out in our tests. As shown in Figure A3, the filtered Δp for Ta040 (dotted line) is generally in phase with the free-stream velocity ($\sim \cos(\omega t)$).

Although the WCS can produce the intended oscillatory flow with a good accuracy, the piston-displacement difference ΔS between a pair of tests is not exactly zero, so we also calculate ΔS using the obtained measurements, i.e.

$$\Delta S = S_r(t) - S_f(t) = \sum_{n=1}^{\infty} \Delta S_n \cos(n\omega t + \varphi_{\Delta sn}) \tag{A1}$$

where ΔS_n and $\varphi_{\Delta sn}$ are amplitude and phase of the n-th harmonic, respectively. As shown in figure A2b for test Ta040, Δs is of O(0.1 mm), which suggests that our flow generation is very accurate (the excursion amplitude for Ta040 is 100 mm). Comparing figure A2a and b, the footprint of facility resonance can be clearly seen in the obtained ΔS. For instance, the oscillations in ΔS and Δp within $\theta = 150^\circ$ to 250° are almost out-of-phase. This implies that the facility resonance also slightly affects flow generation. The water pressure for driving the free-stream oscillatory flow in the WCS is given by the potential flow theory, i.e., equation (4). A non-zero ΔS leads to different u_∞ between a pair of tests, and therefore leads to an additional pressure difference, Δp_a. With the obtained ΔS, Δp_a can be estimated by integrating

$$\frac{\partial}{\partial t}(\Delta u_\infty) = -\frac{1}{\rho}\frac{\partial}{\partial x}(\Delta p_a) \tag{A2}$$

from the free water surface in the open riser to the bottom of the piston-end riser, where the pressure transducers are located. Here Δu_∞ is converted from ΔS using the principle

of volume conservation. The complex amplitude of the n-th Fourier component of Δp_a is

$$\Delta {p_a}^{(n)} = 47(n\omega)^2 \Delta S_n e^{i(\Delta\varphi_{sn}+\pi)} \tag{A3}$$

where the unit of ΔS_n is [mm] and 47 [Pa/mm] is obtained after integration. Figure A2c compares the amplitude of $\Delta {p_a}^{(n)}$ to that of $\Delta p^{(n)}$ for test Ta040. For the dominant 1st-harmonic component, $\Delta {p_a}^{(1)}$ (0.06 Pa) is much smaller than $\Delta p^{(1)}$ (218 Pa), indicating that the primary flow is generated perfectly. However, for higher-order harmonics (above the 3rd harmonic), the correction term becomes non-negligible, especially for the even-order harmonics (e.g. 2nd and 4th harmonics), which theoretically should be zero. The peak of $\Delta {p_a}^{(n)}$ is located around $f = 1$ Hz, which is controlled by facility resonance. This confirms that the facility's resonance affects the flow generation. $\Delta {p_a}^{(n)}$ is significantly smaller than $\Delta p^{(n)}$ around $f = 1$ Hz, so the obtained large value of $\Delta p^{(n)}$ is only partly due to imperfect flow generation, and is mostly due to the sidewall vibration. For each harmonic of the filtered Δp, $\Delta {p_a}^{(n)}$ is subtracted to correct for imperfect flow generation, and the time series of Δp is reconstructed. As shown in figure A3, this correction (the dashed line) significantly reduces some high-frequency components, especially for the 2nd and 4th harmonics. Most importantly, it makes the two half cycles quite symmetric, which is expected for all of our tests. We can further remove all even harmonics. This will not lead to a significant difference, e.g. in figure A3 for Ta040 the dashed and the solid lines (with or without even harmonics) are quite similar, since most of the even harmonics have already been removed after subtracting Δp_a.

Acknowledgments. This research is supported by the National Research Foundation (NRF), Prime Minister's Office, Singapore under its Campus for Research Excellence and Technological Enterprise (CREATE) programme. The Center for Environmental Sensing

and Modeling (CENSAM) is an interdisciplinary research group (IRG) of the Singapore MIT Alliance for Research and Technology (SMART) centre. The authors also gratefully acknowledge the financial support from the Tier-1 research project funded by the Ministry Of Education of Singapore (WBS: R-302-000-126-112).Numerical information is provided in the dataset attached as supporting information.

References

Bagnold, R. A., and G. Taylor (1946), Motion of waves in shallow water. interaction between waves and sand bottoms, *Proceedings of the Royal Society of London. Series A, Mathematical and Physical Sciences*, pp. 1–18.

Barr, B. C., D. N. Slinn, T. Pierro, and K. B. Winters (2004), Numerical simulation of turbulent, oscillatory flow over sand ripples, *Journal of Geophysical Research: Oceans*, *109*(C9).

Blondeaux, P., P. Scandura, and G. Vittori (2004), Coherent structures in an oscillatory separated flow: numerical experiments, *Journal of Fluid Mechanics*, *518*, 215–229, doi: doi:10.1017/S0022112004000953.

Carstens, M., F. Neilson, and H. Altinbilek (1969), *Bed Forms Generated in the Laboratory Under an Oscillatory Flow: Analytical and Experimental Study, Tech. Memo. 28*, U.S. Army Corps of Engineers, Coastal Engineering Research Center.

Fredsøe, J., K. H. Andersen, and B. Mutlu Sumer (1999), Wave plus current over a ripple-covered bed, *Coastal Engineering*, *38*(4), 177–221, doi:10.1016/s0378-3839(99)00047-2.

Grant, W. D., and O. S. Madsen (1982), Movable bed roughness in unsteady oscillatory flow, *Journal of Geophysical Research: Oceans*, *87*(C1), 469–481, doi:

10.1029/JC087iC01p00469.

Grigoriadis, D. G. E., A. A. Dimas, and E. Balaras (2012), Large-eddy simulation of wave turbulent boundary layer over rippled bed, *Coastal Engineering*, *60*, 174–189, doi:10.1016/j.coastaleng.2011.10.003.

Hare, J., A. E. Hay, L. Zedel, and R. Cheel (2014), Observations of the space-time structure of flow, turbulence, and stress over orbital-scale ripples, *Journal of Geophysical Research: Oceans*, *119*(3), 1876–1898, doi:10.1002/2013JC009370.

Hay, A. E., L. Zedel, R. Cheel, and J. Dillon (2012), On the vertical and temporal structure of flow and stress within the turbulent oscillatory boundary layer above evolving sand ripples, *Continental Shelf Research*, *46*(0), 31–49, doi:10.1016/j.csr.2012.02.009.

Holmedal, L. E., D. Myrhaug, and H. Rue (2003), The sea bed boundary layer under random waves plus current, *Continental Shelf Research*, *23*(7), 717–750.

Humbyrd, C. J. (2012), Turbulent combined wave-current boundary layer model for application in coastal waters, Master's thesis, Massachusetts Institute of Technology, Cambridge, MA, U.S.

Jensen, B. L., B. M. Sumer, and J. Fredsøe (1989), Turbulent oscillatory boundary layers at high reynolds numbers, *Journal of Fluid Mechanics*, *206*, 265–297.

Jonsson, I. G. (1966), Wave boundary layer and friction factors, in *Proceedings of the 10th International Conference on Coastal Engineering*, pp. 127–148, ASCE.

Kajiura, K. (1968), A model of bottom boundary layer in water waves, *Bull. Earthquake Res. lnst., Univ. Tokyo*, *46*, 75–123.

Lofquist, K. E. (1980), Measurements of oscillatory drag on sand ripples, in *Proceedings of the 17th International Conference on Coastal Engineering*, pp. 3087–3106, ASCE.

838 Longuet-Higgins, M. S. (1981), Oscillating flow over steep sand ripples, *Journal of Fluid*
839 *Mechanics*, *107*, 1–35.

840 Madsen, O. S. (1993), *Sediment transport outside the surf zone*, Technical Report U.S.
841 Army Engineer Waterways Experiment Station.

842 Madsen, O. S. (1994), Spectral wave-current bottom boundary layer flows, in *Proceedings*
843 *of the 24th International Conference on Coastal Engineering*, pp. 384–398, ASCE.

844 Mathisen, P. P. (1989), Experimental study on the response of fine sediments to wave
845 agitation and associated wave attenuation, Master's thesis, Massachusetts Institute of
846 Technology, Cambridge, MA, U.S.

847 Nichols, C., and D. Foster (2007), Fullscale observations of waveinduced vortex generation
848 over a rippled bed, *Journal of Geophysical Research: Oceans*, *112*(C10).

849 Nielsen, P. (1983), Analytical determination of nearshore wave height variation due to
850 refraction shoaling and friction, *Coastal Engineering*, *7*(3), 233–251.

851 Nikuradse, J. (1933), Strömungsgesetze in rauhen rohren, *Ver. Dtsch. Ing. Forsch.*, *361*.

852 O'Donoghue, T., J. S. Doucette, J. J. van der Werf, and J. S. Ribberink (2006), The
853 dimensions of sand ripples in full-scale oscillatory flows, *Coastal Engineering*, *53*(12),
854 997–1012, doi:http://dx.doi.org/10.1016/j.coastaleng.2006.06.008.

855 Rankin, K. L., and R. I. Hires (2000), Laboratory measurement of bottom shear stress
856 on a movable bed, *Journal of Geophysical Research: Oceans*, *105*(C7), 17,011–17,019,
857 doi:10.1029/2000JC900059.

858 Rodrguez-Abudo, S., and D. L. Foster (2017), Direct estimates of friction factors for
859 a mobile rippled bed, *Journal of Geophysical Research: Oceans*, *122*(1), 80–92, doi:
860 10.1002/2016JC012055.

Rosengaus, M. (1987), Experimental study on wave generated bedforms and resulting wave attenuation, Sc.d. thesis, Massachusetts Institute of Technology, Cambridge, MA, U.S.

Scandura, P., G. Vittori, and P. Blondeaux (2000), Three-dimensional oscillatory flow over steep ripples, *Journal of Fluid Mechanics*, *412*, 355–378, doi: doi:10.1017/S0022112000008430.

Sleath, J. F. A. (1982), Friction coefficients of rippled beds in oscillatory flow, *Continental Shelf Research*, *1*(1), 33–47, doi:https://doi.org/10.1016/0278-4343(82)90031-0.

Swart, D. H. (1974), *Offshore sediment transport and equilibrium beach profiles*, Delft Hydraul. Lab. Publ. 131, Delft.

Treloar, P. D., and C. L. Abernethy (1978), Determination of a bed friction factor for botany bay, australia, *Coastal Engineering*, *2*(Supplement C), 1–20.

van der Werf, J. J., J. S. Doucette, T. O'Donoghue, and J. S. Ribberink (2007), Detailed measurements of velocities and suspended sand concentrations over full-scale ripples in regular oscillatory flow, *Journal of Geophysical Research: Earth Surface*, *112*(F2), F02,012, doi:10.1029/2006JF000614.

Wikramanayake, and Madsen (1994), *Calculation of Movable Bed Friction Factors, Technical Report No.2, Dredging Research Program*, U.S. Army Corps of Engineers, Coastal Engineering Research Center.

Yuan, J., and O. S. Madsen (2014), Experimental study of turbulent oscillatory boundary layers in an oscillating water tunnel, *Coastal Engineering*, *89*, 63–84, doi: http://dx.doi.org/10.1016/j.coastaleng.2014.03.007.

Yuan, J., and O. S. Madsen (2015), Experimental and theoretical study of wave-current turbulent boundary layers, *Journal of Fluid Mechanics*, *765*, 480–523, doi: doi:10.1017/jfm.2014.746.

Yuan, J., D. Wang, and O. S. Madsen (2017), A laser-based bottom profiler system for measuring net sediment transport rates in an oscillatory water tunnel, in *Coastal Dynamics, 2017*, pp. 1495–1505.

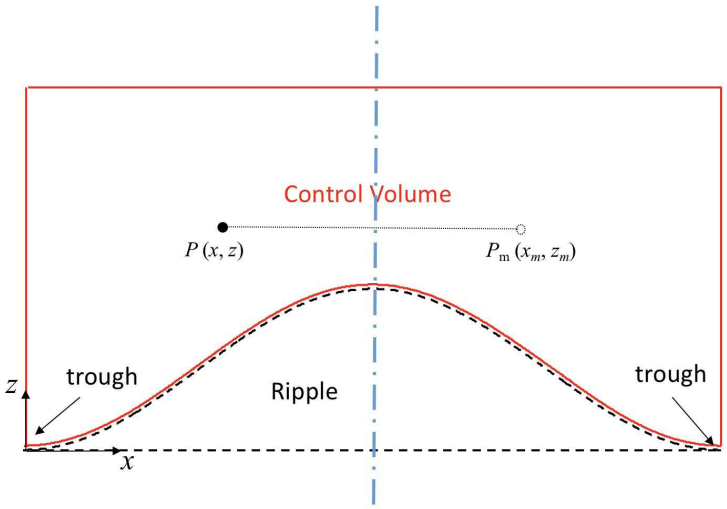

Figure 1. Illustrative drawing for the flow field of interest around one vortex ripple.

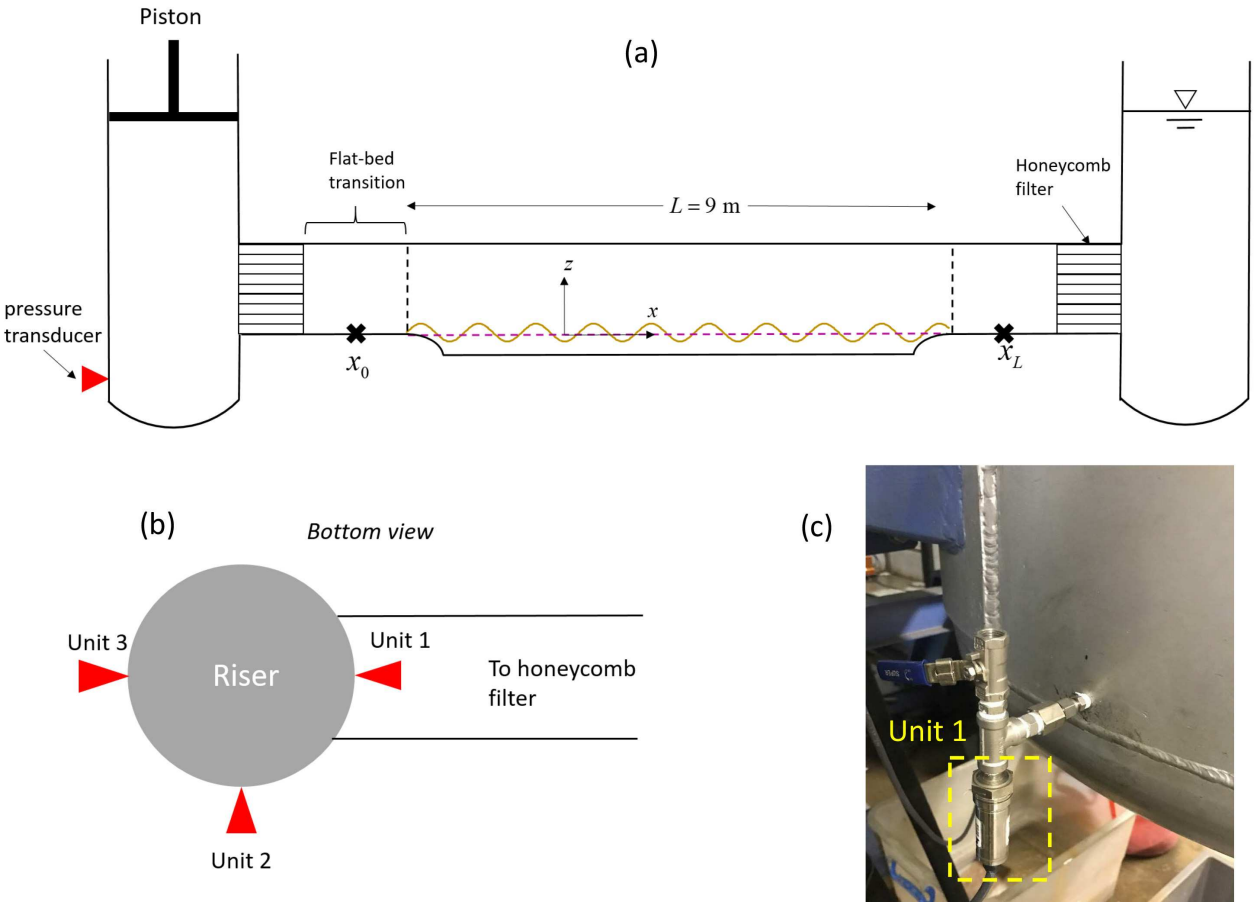

Figure 2. Experimental facility and pressure transducer: (a) illustrative sketch (side view) of the WCS, (b) sketch of pressure transducer's location, (c) photo of pressure transducer.

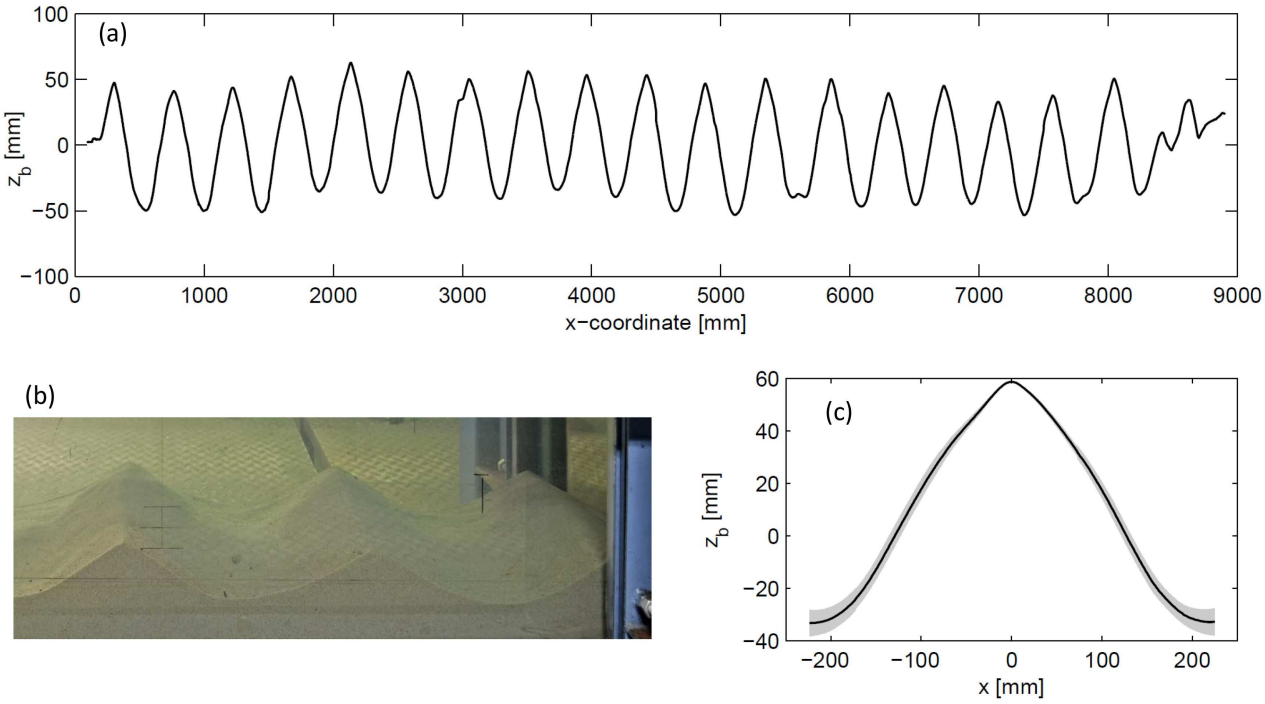

Figure 3. Ripple profile for test Ta040: (a) LBP measurement of the 9 m-long movable bed, (b) side-view photo, (c) ensemble-averaged ripple.

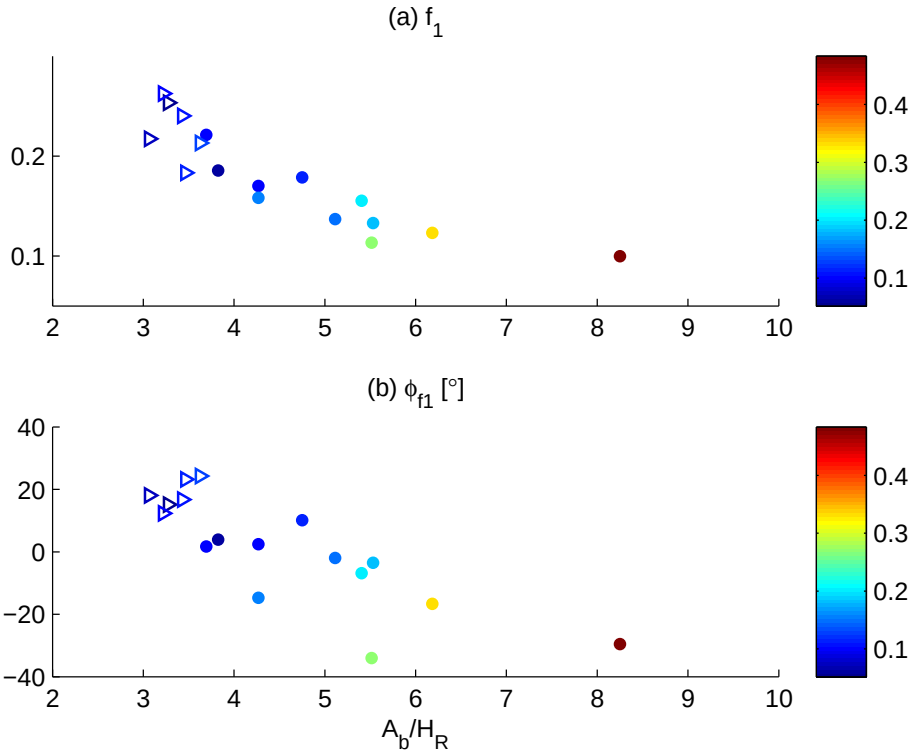

Figure 4. Amplitude and phase of first-harmonic friction factor (the open triangles are from *Lofquist* [1980], and the full circles are from this study. The marker color indicates Shields parameter ψ_{wmd}).

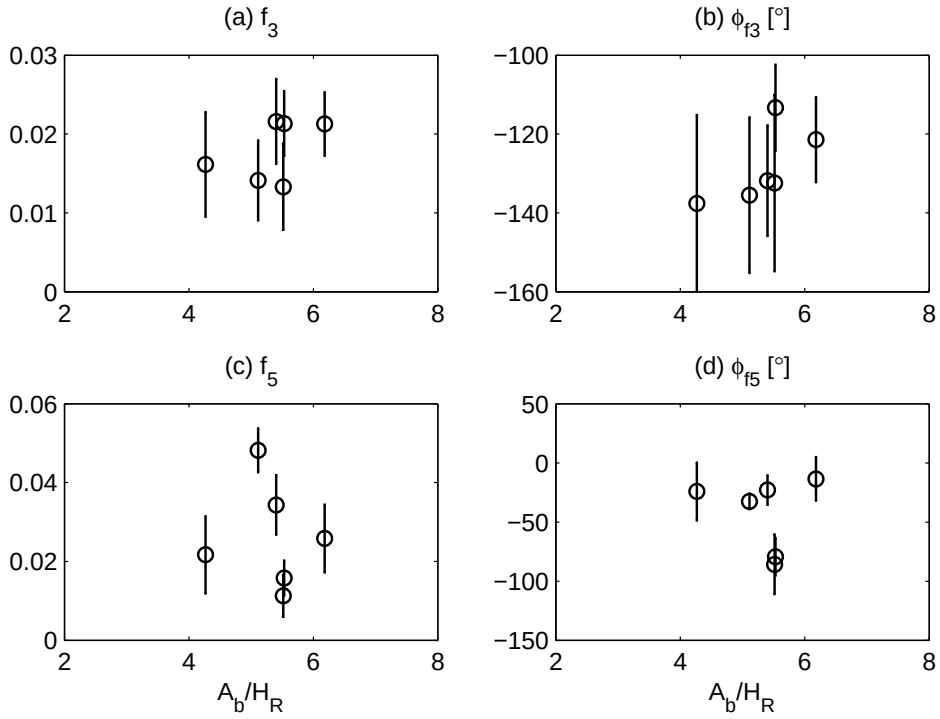

Figure 5. 3rd- and 5th-harmonic friction factors: (a) and (c) are amplitudes, (b) and (d) are phases.

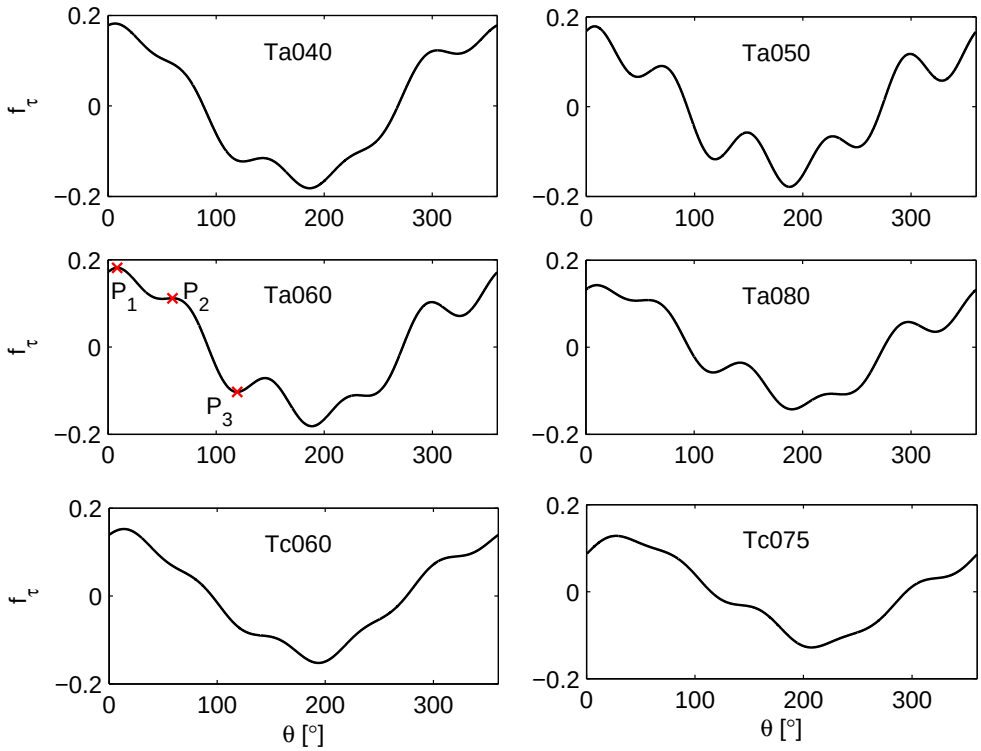

Figure 6. Friction factor f_τ throughout a flow cycle for six tests with acceptable higher-order harmonics.

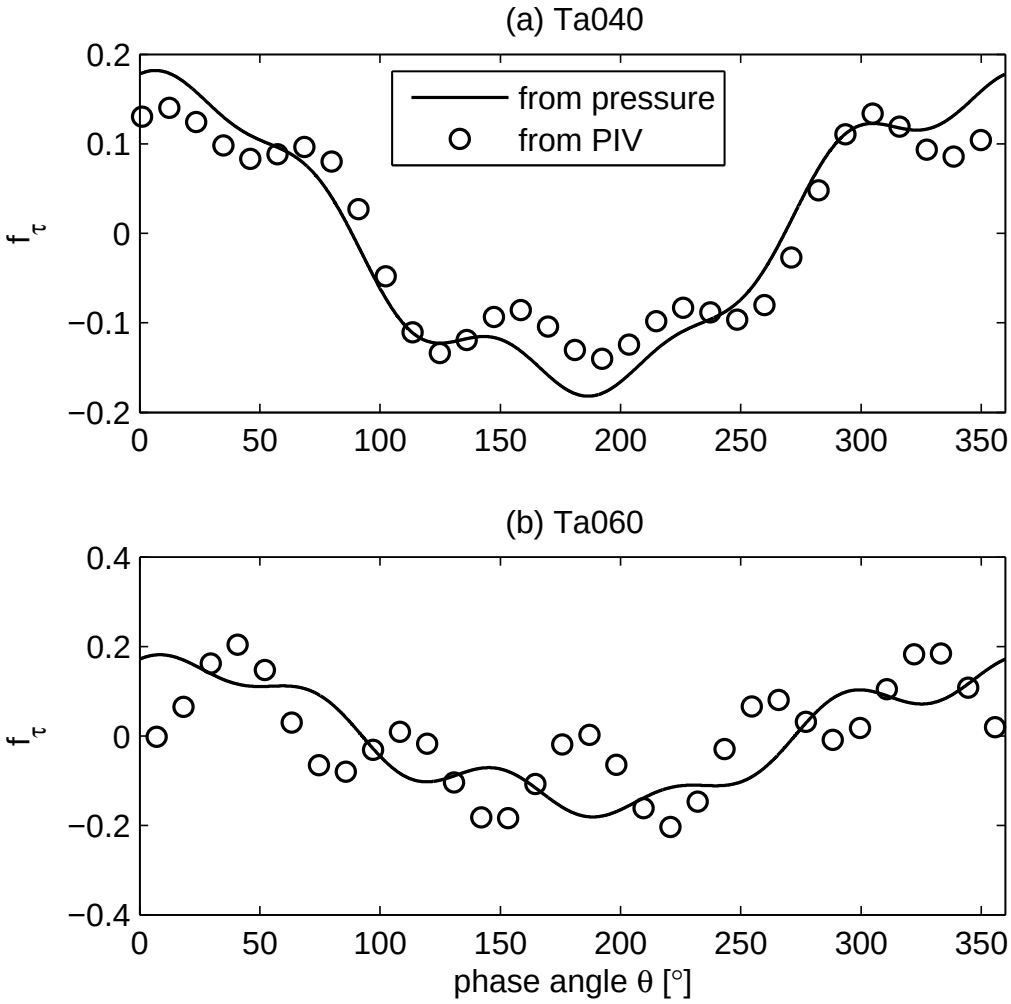

Figure 7. Intra-period variation of friction factor f_τ obtained from pressure and PIV measurements: (a) test Ta040, (b) test Ta060

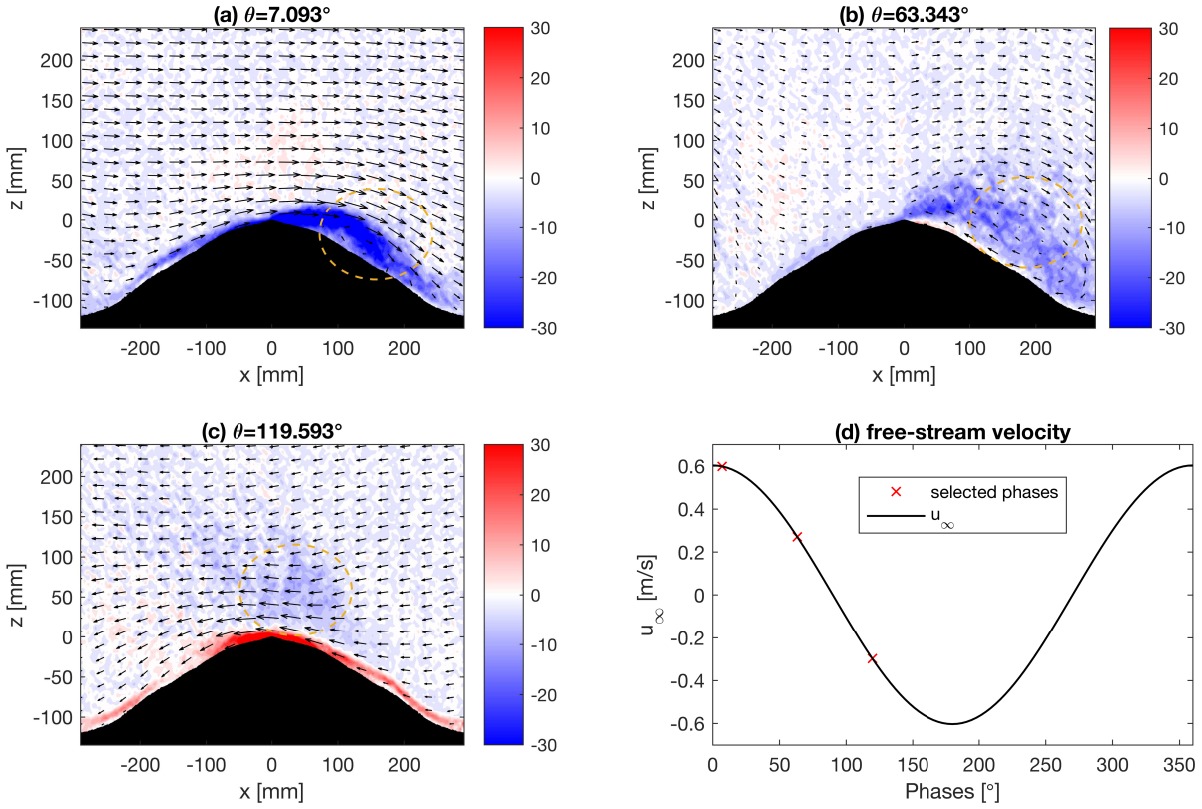

Figure 8. PIV measurements of flow velocity and normalized vorticity ($\omega_y^* = \omega_y T/2\pi$) for test Ta060 at three representative phases (the main coherent vortex of interest is highlighted by the dashed circles).

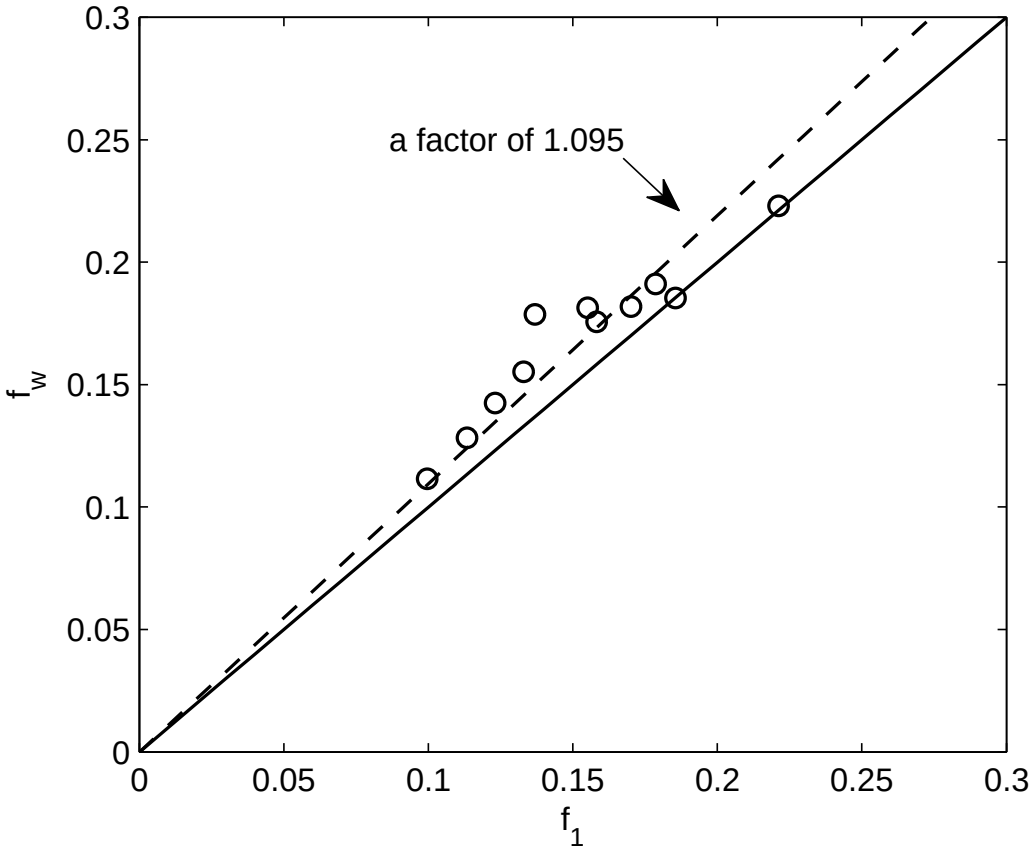

Figure 9. Comparisons between wave friction factor (f_w) and first-harmonic (f_1) friction factor (solid line indicates perfect agreement and the dashed line is a fitting through the origin).

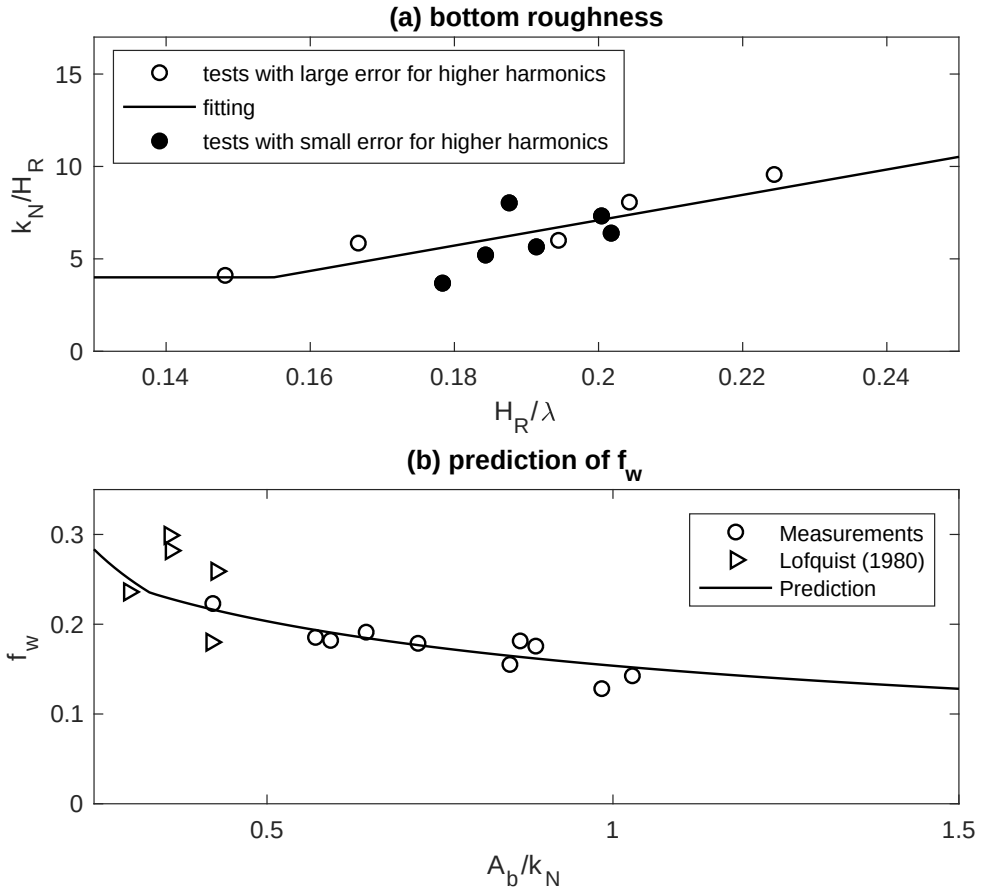

Figure 10. Equivalent sand-grain roughness and prediction of wave friction factor

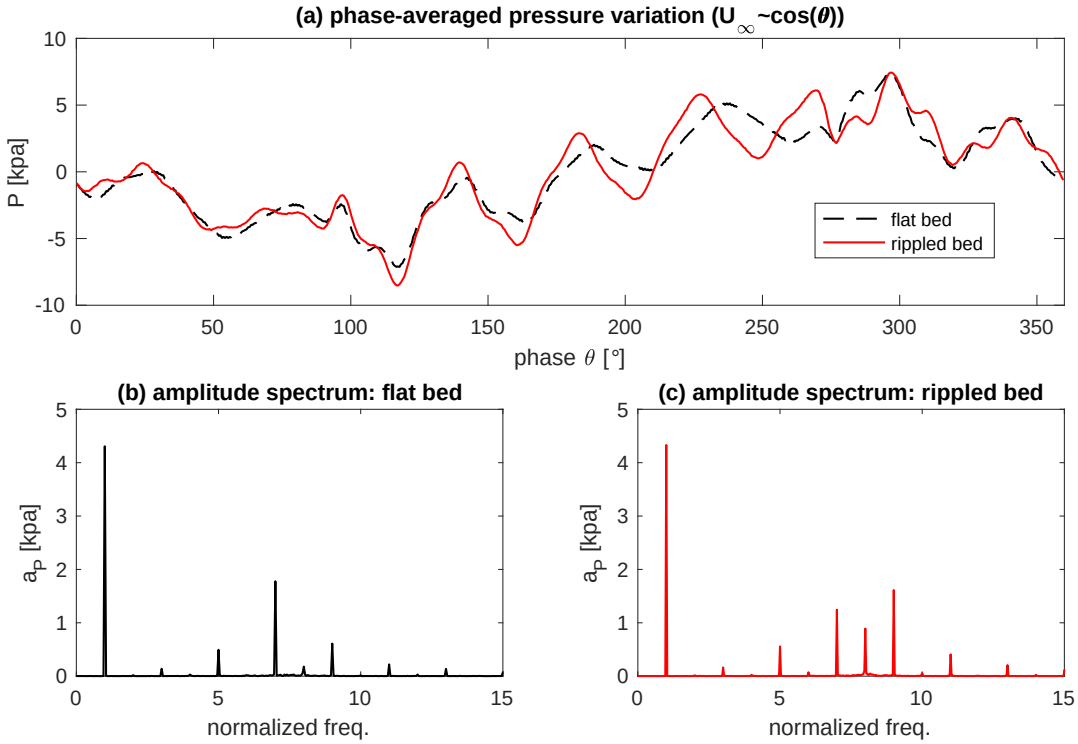

Figure A1. Water pressure for test Ta040 over flat and rippled beds: (a) intra-period variation, (b) amplitude spectrum for flat-bed condition, (c) amplitude spectrum for rippled-bed condition.

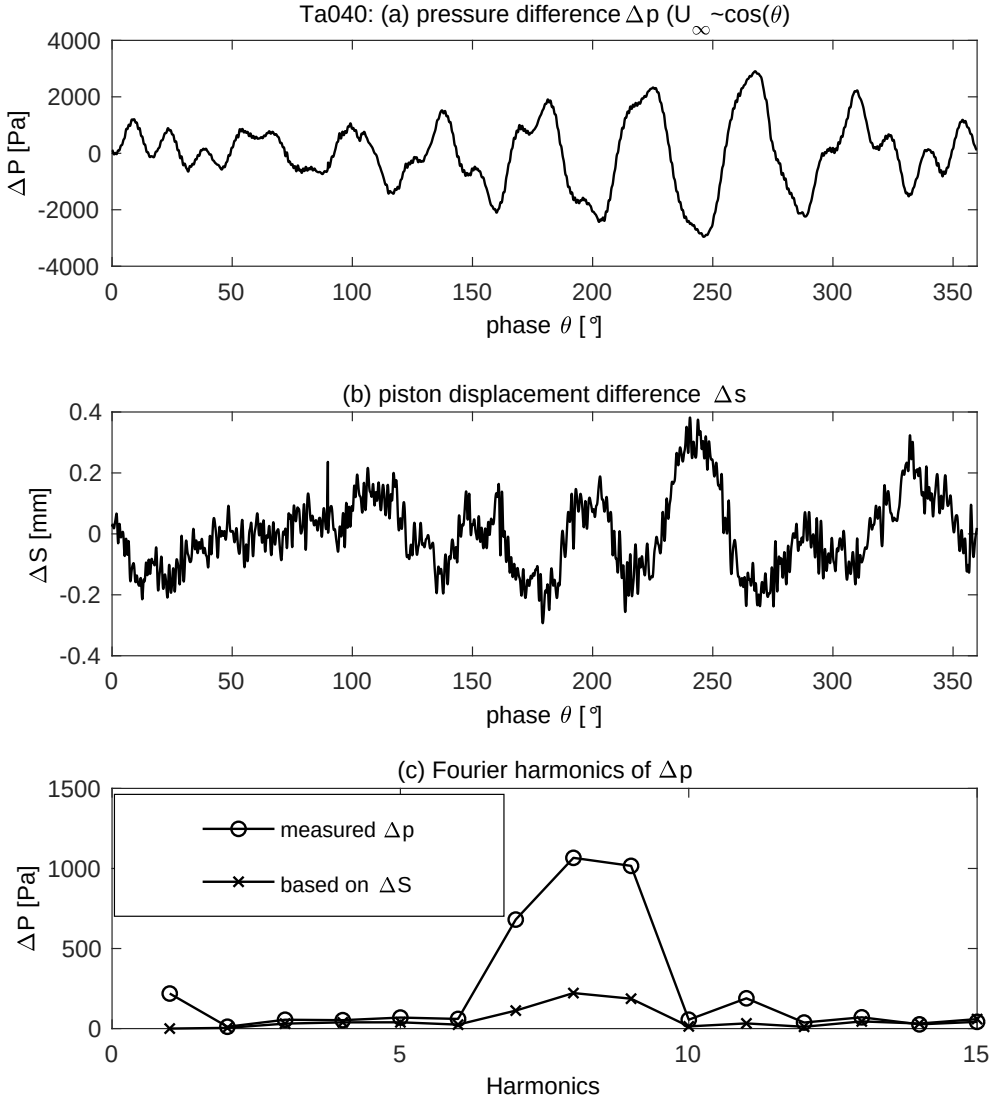

Figure A2. Pressure difference and piston-displacement difference for test Ta040: (a) raw pressure difference, (b) piston-displacement difference, (c) amplitude spectra for pressure difference.

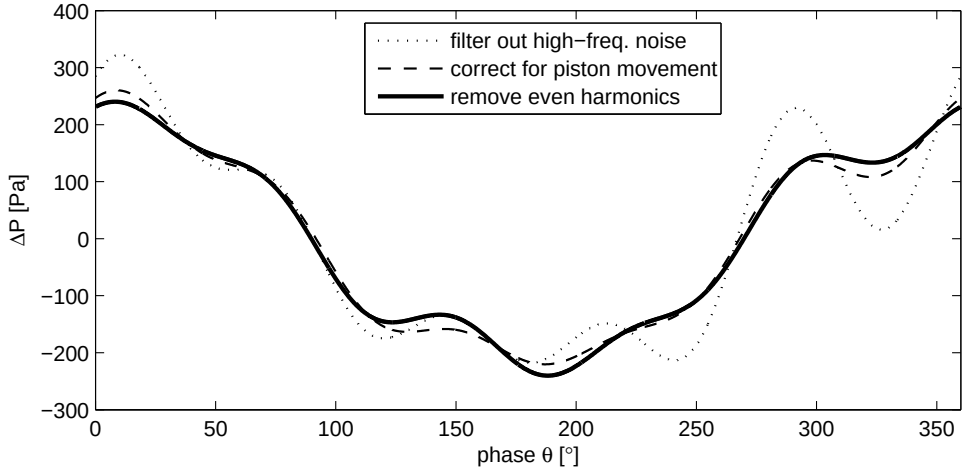

Figure A3. Corrected pressure difference for test Ta040.

Table 1. Test conditions

Test ID	A_b [m]	T [s]	ψ_{wmd}	U_∞ [m/s]	H_R [mm]	λ [mm]	No. of ripples	duration [h]	Re_w
Ta030	0.30	6.25	0.064	0.302	77	396	21	4.0	$9.1 \cdot 10^4$
Ta040	0.40	6.25	0.105	0.402	92	456	18	3.2	$1.6 \cdot 10^5$
Ta050	0.50	6.25	0.153	0.503	96	479	17	1.4	$2.5 \cdot 10^5$
Ta060	0.60	6.25	0.21	0.603	109	581	14	1.0	$3.6 \cdot 10^5$
Ta080	0.80	6.25	0.344	0.804	127	689	12	0.5	$6.4 \cdot 10^5$
Ta100	1.00	6.25	0.506	1.005	119	803	11	0.3	$1.0 \cdot 10^6$
Tc045	0.60	8.33	0.118	0.452	124	607	13	1.1	$2.7 \cdot 10^5$
Tc060	0.80	8.33	0.194	0.603	142	742	12	0.8	$4.8 \cdot 10^5$
Tc075	1.00	8.33	0.285	0.754	178	998	9	0.3	$7.5 \cdot 10^5$
Td044	0.70	10	0.107	0.44	186	829	10	3.3	$3.1 \cdot 10^5$
Td057	0.90	10	0.165	0.565	207	1242	7	1.5	$5.1 \cdot 10^5$

Table 2. Fourier components of normalized total bottom shear stress

Test ID	1st harmonic				3rd harmonic				5th harmonic			
	f_1	Δf_1*	$\phi_{f1}[^\circ]$	$\Delta\phi_{f1}[^\circ]$	f_3	Δf_3	$\phi_{f3}[^\circ]$	$\Delta\phi_{f3}[^\circ]$	f_5	Δf_5	$\phi_{f5}[^\circ]$	$\Delta\phi_{f5}[^\circ]$
Ta030	0.185	5.8%	3.9	3.3	0.013	76.3%	-88.6	37.4	0.010	134.7%	97.8	180.0
Ta040 (s)	0.170	3.5%	2.4	2.0	0.016	41.2%	-137.6	22.4	0.022	45.1%	-24.2	24.3
Ta050 (s)	0.137	3.6%	-2.0	2.0	0.014	35.8%	-135.5	19.7	0.048	11.5%	-32.5	6.6
Ta060 (s)	0.155	2.7%	-6.8	1.5	0.022	25.0%	-131.8	14.0	0.034	22.0%	-22.9	12.4
Ta080 (s)	0.123	3.0%	-16.7	1.7	0.021	19.0%	-121.4	10.8	0.026	33.3%	-13.6	18.4
Ta100	0.100	2.3%	-29.5	1.3	0.013	22.5%	-134.3	12.7	0.006	103.3%	-81.7	180.0
Tc045	0.179	4.0%	10.1	2.3	0.014	60.2%	-144.5	31.0	0.029	29.6%	-53.5	16.5
Tc060 (s)	0.133	2.4%	-3.5	1.3	0.021	19.3%	-113.3	10.9	0.016	28.1%	-79.4	15.7
Tc075 (s)	0.113	4.2%	-34.0	2.4	0.013	41.1%	-132.4	22.3	0.011	47.0%	-85.8	25.2
Td044	0.221	7.9%	1.7	4.5	0.016	182.4%	48.0	180.0	0.025	92.0%	-136.3	42.6
Td057	0.158	11.3%	-14.7	6.5	0.006	157.1%	-159.9	180.0	0.020	45.0%	-134.3	24.2

Table 3. Comparison between PIV-based and pressure-based measurements of first-harmonic total bottom shear stress

Test ID	f_1		$\phi_{f1}[^\circ]$	
	Pressure	PIV	Pressure	PIV
Ta040	0.17	0.14	9.7	-1.4
Ta060	0.16	0.12	-6.8	6.6